Journal of Building Engineering 83 (2024) 108415

Contents lists available at ScienceDirect

Journal of Building Engineering

journal homepage: www.elsevier.com/locate/jobe

Parametric study of reinforced interlocking brick wall under cyclic loading

Guanyu Xie [a], Xihong Zhang [a,*], Hong Hao [a,b,**], Joyis Thomas [c]

[a] Centre for Infrastructural Monitoring and Protection, School of Civil and Mechanical Engineering, Curtin University, Bentley, WA, 6102, Australia
[b] Earthquake Engineering Research and Test Centre, Guangzhou University, Guangzhou, China
[c] Tetraloc Pty Ltd, Bellevue, WA, 6056, Australia

ARTICLE INFO

Keywords:
Interlocking brick
Mortarless
Lateral strength
Deformation capacity
Energy dissipation

ABSTRACT

Mortarless interlocking brick walls are a new form of masonry structures that can be efficiently constructed. In this study, a detailed numerical model of an interlocking brick wall under quasi-static in-plane cyclic loading is generated and verified with laboratory test data. The influence of the vertical reinforcement placement methods, i.e., grouted vs. unbonded, and the influence of wall-to-brick size ratio are firstly investigated. Parametric studies are then carried out to quantify the influences of axial precompression level, shear span ratio and friction coefficient between bricks on the lateral load-carrying capacity, deformation capacity, and energy dissipation capability of the studied mortarless interlocking brick walls subjected to in-plane cyclic loading with analytical equations summarised for predicting the resistance performance of this type of mortarless interlocking brick walls under in-plane cyclic loading.

1. Introduction

Mortarless interlocking masonry structures have been gaining attention in recent years. This is because compared with conventional masonry structures, interlocking bricks are self-aligned and require no mortar in construction. Hence, much less labour skills are required to construct interlocking masonry and the construction efficiency is also greatly enhanced [1–3]. Because of the interlocking mechanism, the connection between bricks provides different resistances to loadings compared to those of conventional mortar-bonded masonry [4,5]. For example, Sturm et al. [6] performed shear tests on interlocking bricks with relatively shallow interlocking keys, which were found to ameliorate the shear strength considerably. Another feature of the interlocking masonry structures is their high energy dissipation capability. Previous studies found that the stacked interlocking bricks tend to slide along the interlocking keys under lateral loading, which leads to significant frictional energy dissipation [6,7]. Unlike in conventional masonry walls where little inter-brick movement is allowed before decohesion of the mortar-brick interface, relative movements of interlocking bricks occur when the mortarless interlocking masonry structure is still elastic [8,9]. Therefore, the material damage of interlocking masonry structures is delayed [8].

Because of the above differences between interlocking bricks and conventional bricks, under seismic loading, different response and damage modes are reported. For conventional masonry walls, diagonal cracking dominates, which usually results from the relatively low shear strength of the brick-mortar interfaces [10,11]. By contrast, most types of interlocking bricks are designed to

* Corresponding author.
** Corresponding author.
E-mail addresses: guanyu.xie@student.curtin.edu.au (G. Xie), xihong.zhang@curtin.edu.au (X. Zhang), hong.hao@curtin.edu.au (H. Hao), joyis.thomas@tetraloc.com (J. Thomas).

https://doi.org/10.1016/j.jobe.2023.108415
Received 15 May 2023; Received in revised form 28 November 2023; Accepted 28 December 2023
Available online 30 December 2023

provide interlock in horizontal directions (both in-plane and out-of-plane) but not in the vertical direction [12]. Therefore, no vertical tensile strength exists in the mortarless interlocking masonry walls, which leads to a relatively low flexural resistance if no strong anchorage is provided by vertical reinforcements. With the stronger shear strength and the weaker flexural resistance, rocking tends to occur on interlocking brick walls, as observed in the shaking table tests on mortarless interlocking brick wall conducted by Xie et al. [13,14], which could potentially lead to severe toe brick crushing.

Abundant research has been conducted on the performance of conventional masonry structures in the aspects of strength and deformability, whose results have been incorporated in many masonry design codes. For example, it is pointed out that the lateral strength of a conventional masonry wall is usually contributed from three sources, i.e., the masonry material strength, the strength enhancement related to axial loading, and the strength provided by horizontal reinforcement [15,16]. Hence, in several commonly used standards, the lateral strength of masonry walls is expressed as a linear combination of the above three factors [17–20]. Moreover, "masonry patterns" have also been recognised to influence the load-bearing capacity. Celano et al. [21] distinguished masonry patterns into 'regular' and 'irregular' and summarised the equations for predicting their shear capacities respectively. Szabó et al. [22] outlined a series of indices for quantitatively measure masonry patterns to assess the structural performance of masonry structures more accurately. The deformation capacity of masonry walls has also been studied by many researchers. Petry and Beyer [23] summarised the drift limit for unreinforced masonry (URM) walls prescribed in different standards and investigated the influence of shear span ratios, axial precompression ratios and size effect on the in-plane drift capacity of URM walls, which is further studied by Dolatshahi et al. [24] through numerical simulations in more complicated scenarios. Other researchers [25–28] focused on the factors influencing the drift capacity of reinforced masonry (RM) walls and concluded that RM walls with shear-dominated failure tends to be brittle compared to the ones with flexure-dominated failure. Nonetheless, as pointed out by Morandi and Magenes [29], the performance of a masonry wall, especially its deformation capability, is largely related to the type of masonry units and joints. Hence, the applicability of the current understandings for masonry walls based on conventional masonry needs to be investigated on mortarless interlocking masonry made of specific interlocking bricks.

Some studies have been conducted on the performance of mortarless interlocking brick structures. Shi et al. [4,5] investigated the compressive and shear behaviours of interlocking brick prisms using a specific type of interlocking bricks. The influences of material strength, number of bricks, axial precompression, etc. were all quantified. In a similar vein, Dorji et al. [30] conducted a series of tests to characterise the compressive and tensile behaviours of mortarless masonry units, observing that the stress–strain behaviour of ungrouted prisms was less stiff than that of grouted prisms. Considering the use of reinforcement in engineering practice, Zahra et al. [31] studied the axial compression characteristics of reinforced mortarless masonry (RMM) wall panels and proposed an empirical formulation for computing the mortarless masonry strength based on the block strength. Zahra et al. [32] also investigated the influence of reinforcement ratio on the in-plane and out-of-plane behaviour of mortarless masonry, concluding that higher reinforcement ratios lead to higher in-plane and out-of-plane lateral strengths of mortarless masonry due to the dowel action. The influence of contact imperfections in the static behaviour of mortarless masonry was also studied. Through Monte-Carlo simulations, Shi et al. [103] investigated the influence of the size and distribution of the geometric imperfections in bricks on the compressive performance of mortarless interlocking brick walls, including the crack distribution, load transfer paths, and compressive strength of the walls. Zahra and Dhanasekar [33] characterised and proposed mitigation strategies for the contact surface roughness in mortarless masonry, showing that techniques like grinding and the use of filler material can effectively reduce peak contact pressure. As for the seismic behaviour of mortarless interlocking brick structures, Bland and Qu et al. [34,35] conducted in-plane cyclic loading tests on reinforced mortarless interlocking brick walls and summarised the influence of aspect ratio on the lateral strength and ductility qualitatively. Kohail et al. [12,36] conducted in-plane cyclic loading tests on walls made of two types of interlocking bricks and conventional masonry units (CMUs), respectively, and observed different behaviour of the two kinds of interlocking brick walls, demonstrating that the geometric shape of interlocking bricks has a vital influence. Gul et al. [37] conducted a cyclic test on an unconfined mortarless interlocking masonry building, and found although the equivalent damping ratio of the mortarless interlocking masonry structure decreased due to surface wear and tear of each individual brick during the tests, its average equivalent damping ratio was still 50% higher compared to conventional masonry structures. To further ameliorate the seismic performance of the mortarless interlocking masonry structure, Gul et al. [38] added confinement at the corners of the studied mortarless interlocking masonry building and conducted a cyclic test on it. It proved that both the load and deformation capacity of the confined structure were significantly enhanced compared to its unconfined counterpart. Xie et al. [39] conducted cyclic test on a mortarless wall made of the same type of interlocking bricks as used in this study, revealed the damage development mechanism of the wall by digital image correlation (DIC) technique and proved its significant deformation capability. Shaking table tests have also been conducted on mortarless interlocking masonry structures by some researchers [9,13,14,40]. Inter-brick movements, including sliding and pounding, occurred under seismic loading and dissipated significant amount of energy. Recently, the performance of mortarless interlocking masonry structures under blast loads has also attracted the attention of researchers [41–43]. In a blast loading test on a confined mortarless interlocking masonry wall conducted by Ullah et al. [43], the interlocking masonry units demonstrated their ability to resist blast loads in the out-of-plane direction through the interlocking between the keys. Nevertheless, the above tests concentrated only on specific designs and did not expand the discussions to general cases with varying design parameters owing to the limited number of tests that could be carried out on a structural scale.

Overall, the behaviour and performance of mortarless interlocking masonry structures differ from those of conventional masonry structures and even differ among interlocking masonry structures made of different types of interlocking units. Comprehensive understanding and design guidance are still lacking for them.

2. Introduction of the studied interlocking brick

In this study, the cyclic behaviour of mortarless interlocking brick walls made of a specific type of interlocking bricks is studied via numerical simulations. The geometrical dimensions of the studied interlocking brick are displayed in Fig. 1. There are a total of 6 interlocking keys on each brick, with 4 small keys located in the front and 2 relatively larger ones located at the back. There are two 30 mm diameter holes in each brick for vertical reinforcement, as displayed in Fig. 1e. In contrast to most other types of interlocking bricks with distinct one-to-one corresponding protrusions and recesses, the bricks investigated in this study are of a topological interlocking nature [44]. Their various surfaces are interrelated, allowing these bricks to be combined in various configurations while maintaining an interlocking mechanism [44,45], as shown in Fig. 2a–c. The transition between the interlocking keys and the main body of the brick is gentle, which reduces the stress concentration around interlocking keys [46]. When the bricks are assembled, the top and bottom surfaces of these bricks interplay in a manner that geometrically constraints one another in multiple directions, providing both in-plane and out-of-plane stability to the assembly. Fig. 2d–f illustrates the interlocking patterns in different directions when these bricks form a small panel.

The mechanical properties of this type of interlocking bricks including its compressive properties and shear properties were quantified by Shi et al. [4,5]. Under dynamic loading, shaking table tests were conducted on mortarless interlocking brick walls with vertical reinforcement [13]. The test results revealed that under in-plane seismic loads, due to the lack of bonding between the bricks, local oscillation of the bricks occurred, which helped the energy dissipation of the wall. Regarding the overall response, due to the strong shear resistance provided by the interlocking keys of these bricks and the low vertical tensile strength of the wall because of the absence of cohesion and interlocking in the vertical direction, the response was dominated by rocking, subsequently causing toe crushing damage and the spalling of bricks around the toe. However, it should be noted that even after severe toe crushing damage, the wall remained standing. In addition, numerical simulations were conducted to study the response of these mortarless interlocking brick walls under in-plane seismic loads. The results indicate that due to the enhanced shear strength provided by the interlocking keys, these walls can withstand higher in-plane seismic loads compared to their conventional mortar-bonded masonry wall counterparts. However, due to the lack of vertical tensile capacity, these walls are sensitive to vertical seismic loading, whose influence cannot be ignored in their seismic design.

Preliminary in-plane quasi-static cyclic loading test was also conducted [39]. Unlike in the aforementioned shaking table tests, in this experiment, the vertical reinforcement inside the wall was strongly anchored in the top beam and footing, providing significant vertical tensile capacity for the wall. Relative sliding between the bricks was observed which increased with the increase of lateral displacement. Slight rocking was observed at low drift ratio, but due to the anchorage of the vertical reinforcement, the rocking did not continue to develop. As the lateral displacement increased, the wall exhibited a diagonal shear cracking failure mode. However, even after major diagonal shear cracks formed, the lateral load-carrying capacity of the wall continued to increase. This was because the good residual resistance provided by the unique feature of the particular interlocking bricks combined with the confinement of reinforcements prevented the wall from disintegration after the formation of major diagonal shear cracks. The eventual failure of the wall was resulted only after the fracture of the reinforcement.

A comparison was made between this cyclic loading test and an in-plane quasi-static cyclic loading test conducted by Dhanasekar et al. [10,47–49] on a conventional mortar-bonded masonry wall with similar parameters. The results show that although both walls failed in a diagonal shear cracking mode, in the conventional masonry wall, the cracks were primarily due to mortar bonding failure, with less damage to the bricks; moreover, the cracks were mainly concentrated along the path of the diagonal shear cracking while little damage was observed on the rest of the wall. In contrast, in the mortarless interlocking brick wall, due to the absence of mortar joints, material failure was manifested as brick cracking, and the brick damage was widely distributed across the wall, not confined to the vicinity of the diagonal shear cracking paths. Therefore, the latter is significantly more efficient in material utilisation than the former. In addition, the drift ratio at failure for the conventional mortar-bonded masonry wall was 0.44%, while for the mortarless interlocking brick wall it was 3.29%, demonstrating the latter's far superior in-plane deformation capacity. This is because, in the mortarless interlocking brick wall, the relative movements between the bricks contributed to a portion of the wall's lateral deformation. Additionally, at small drift ratios, although major diagonal shear cracks had already appeared, most of the interlocking keys were still effective, allowing the wall to withstand larger lateral displacements. A comparison of the hysteresis curves of the two walls also shows that before reaching peak lateral strength, the mortarless interlocking brick wall exhibited significantly higher energy

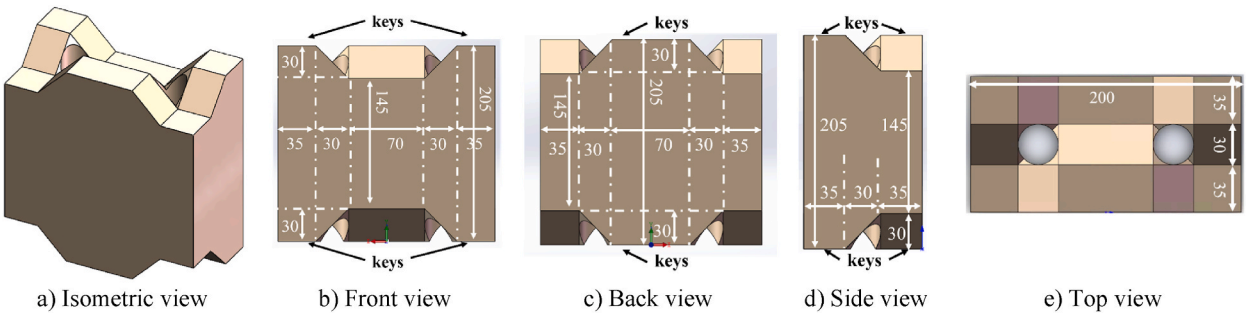

Fig. 1. Geometric dimensions of the studied interlocking brick. a) Isometric view, b) Front view, c) Back view, d) Side view, e) Top view.

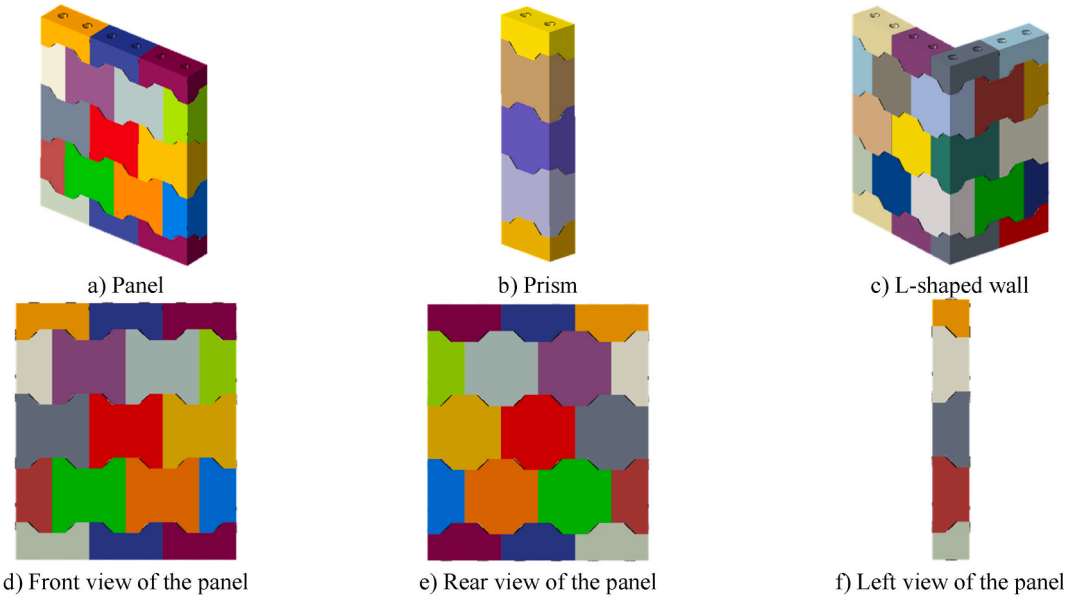

Fig. 2. Assemblies of the studied interlocking bricks. a) Panel, b) Prism, c) L-shaped wall, d) Front view of the panel, e) Rear view of the panel, f) Left view of the panel.

dissipation than the conventional mortar-bonded masonry wall, benefiting from the energy dissipation contributed by the relative movement between the interlocking bricks and the widespread material damage across the entire wall during loading.

To thoroughly understand the behaviour of mortarless interlocking brick walls under cyclic loading, a more systematic study is carried out. A detailed numerical model is established and verified with laboratory testing data [39]. Intensive parametric studies are carried out to quantify the influences of the vertical reinforcement placement methods, i.e., grouted vs. unbonded, wall-to-brick size ratio, axial precompression levels, shear span ratios, and friction coefficients between bricks on the lateral strength, deformation capacity and energy dissipation capability of the wall, with corresponding analytical equations proposed, to facilitate the strength-based design of the studied mortarless interlocking brick wall.

3. Numerical modelling

The commercial finite element software Abaqus/Explicit [50] is used in this study. This section introduces the development of numerical modelling including the boundary conditions of the wall, the meshing of the interlocking bricks, the contact settings and the material constitutive relationship.

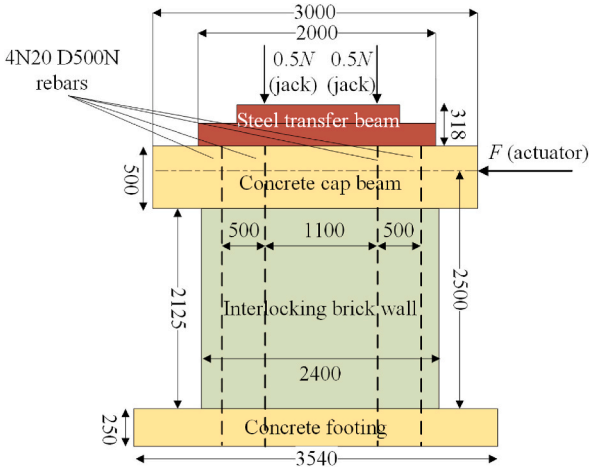

Fig. 3. Test specimen details.

3.1. Model detail and test setup

The model in this study is established based on the in-plane quasi-static cyclic loading experiment conducted on a mortarless interlocking brick wall by Xie et al. [39]. As shown in Fig. 3, the wall is near full-scale, with 2125 mm in height, 2400 mm in length and 100 mm in thickness. It is connected to a concrete footing at its bottom and a concrete cap beam to its top. Both the footing and the cap beam are constructed of reinforced concrete, utilising N40 concrete and D500N reinforcement. The footing measured 3540 mm in length, 300 mm in width, and 250 mm in height, with a longitudinal reinforcement ratio of 2.98%. The cap beam had dimensions of 3000 mm in length, 200 mm in width, and 500 mm in height, with a longitudinal reinforcement ratio of 2.51%. Both beams were reinforced with φ10mm stirrups at 100 mm spacing. The wall was reinforced with 4 pieces of φ20mm D500N rebars, which were anchored to the footing at the bottom and to the cap beam at the top and were left ungrouted against the bricks. To prevent anchorage failure, steel rings were embedded into the footing and cap beam to distribute the anchorage force.

An axial compressive load was slowly applied to the cap beam through a steel load-transfer beam by two vertical hydraulic jacks, as shown in Fig. 3. The steel transfer beam was fabricated by welding a 2000 mm long 250UB 25.7 beam to an 1800 mm long 250UC 72.9 beam, resulting in an overall height of 318 mm. The connection between the steel transfer beam and the concrete cap beam was ensured by 6 M14 bolts. The axial load N applied by the jacks as well as the weight of the upper structure was equivalent to imposing a 0.47 MPa axial precompression (p) on the wall, which was close to the dead load for a three-to-four-storey masonry structure [8, 51–53]. After the wall achieved a stable state under the axial load, the cyclic loading was applied to the cap beam using an actuator with a maximum stroke of ±250 mm and a maximum loading capacity of 1000 kN. The distance between the centre of the actuator loading plate and the wall bottom, i.e., the shear span of the wall [54], was 2500 mm. Table 1 presents the loading protocol for the in-plane quasi-static cyclic loading applied during the experiment. The load was applied in the form of a sinusoidal wave. As per FEMA-461 [55], each loading amplitude was repeated twice. Following previous studies [51,56], the loading speed increased with the rise in displacement amplitude to ensure a consistent period for each loading cycle.

In the numerical model, considering the exorbitant computational resources required for this simulation and the distinctly larger stiffness of components such as the concrete footing, the load-transfer beam, and the cap beam compared to the interlocking brick wall, these components are not explicitly modelled. In reference to Dolatshahi et al. [24], the fixed boundary condition is applied to the bottom of the wall to simulate the restraining effect of the footing on the wall. A reference point O′ is established at the centre of the top of the wall at the height of the actuator, which is connected to the top of the wall by kinematic coupling [57], as shown in Fig. 4. Thus, the axial precompression from the hydraulic jacks and the horizontal load from the hydraulic actuator could be applied to point O′ and then transmitted to the wall via the kinematic coupling. It is worth noting that in such a simplification scheme the distance from point O' to the bottom of the wall is the shear span (H_0), namely the height of the zero bending moment position. The final model comprises a total of 102,865 elements and 158,736 nodes.

In alignment with the experimental loading sequence, the simulation initiates with a gradual application of vertical axial force. Once the axial loading is completed, the quasi-static cyclic loading is introduced. The mass scaling technique is utilised to accelerate the computation. To ensure the accuracy of the simulation and mitigate pronounced dynamic effects, the model's kinetic and internal energies are closely monitored to ensure the former being a small fraction of the latter [58], as shown in Fig. 5.

A mesh size of 17.5 mm is chosen after mesh convergence analyses. As shown in Fig. 6, each brick is meshed into 672 elements. It is worth noting that the circular holes on the brick shown in Fig. 1e are simplified to square holes whose side length equals to the diameter of the circle to improve mesh quality. Previous numerical studies have demonstrated that this simplification has a minimal influence on the overall in-plane response of the wall [13,39]. To account for the large deformations that occur in the wall close to failure and the numerous contacts involved in the simulation, the continuum stress/displacement three-dimensional eight-node reduced-integration element (C3D8R) is chosen as the solid element type for the simulation, as it is suitable for contact analysis and can withstand severe distortions [57,59].

3.2. Material constitutive models

Rammed earth composed of 7 mm aggregates, quarry sand, dry sand, cement, water, etc. is used to produce the interlocking bricks used in the aforementioned test. Uniaxial compressive tests are conducted by the authors on cylinders drilled out of the bricks after a curing period of 28 days. The tests yield a mean uniaxial compressive strength of 20 MPa with a corresponding mean compressive strain of 0.0056 and a mean Young's modulus of 6700 MPa. Additionally, the density of this material is measured to be 2400 kg/m^3. The uniaxial tensile strength of the material is set to one-tenth of its uniaxial compressive strength following previous studies [4,13,

Table 1
Loading protocol.

Displacement at wall top (mm)	Drift ratio (%)	Loading speed (mm/s)	Period (s)
4	0.19%	0.03	480
6	0.28%	0.05	480
10	0.47%	0.08	480
20	0.94%	0.17	480
30	1.41%	0.25	480
40	1.88%	0.33	480
50	2.35%	0.42	480
60	2.82%	0.5	480
70	3.29%	0.58	480

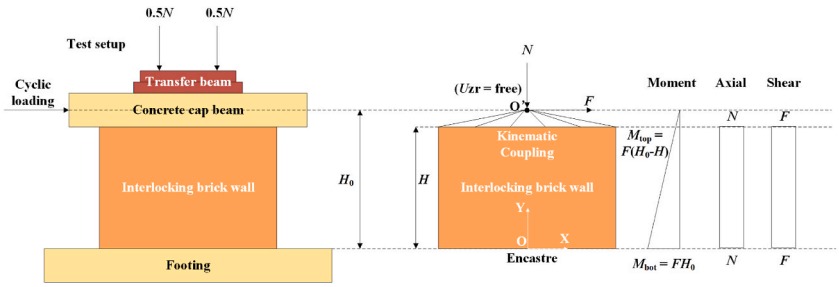

Fig. 4. Simplification scheme of the boundary condition of the wall.

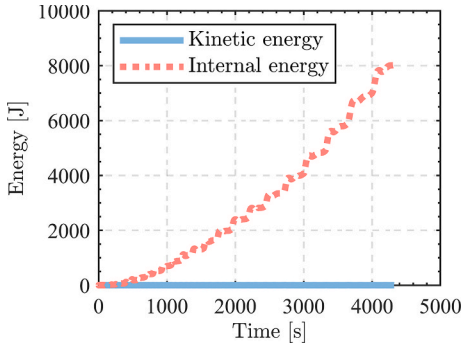

Fig. 5. Comparison of the kinetic energy and internal energy of the model throughout the computation.

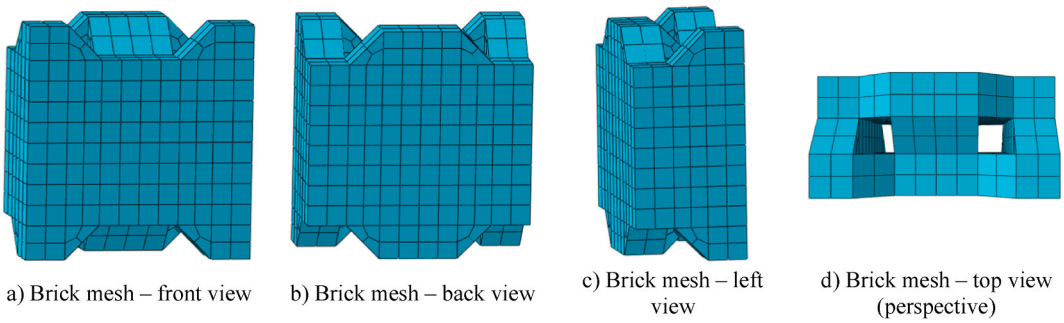

Fig. 6. Mesh of a whole brick. a) Brick mesh – front view, b) Brick mesh – back view, c) Brick mesh – left view, d) Brick mesh – top view (perspective).

60]. These values are subsequently incorporated into the constitutive model for the brick material in the numerical simulations.

To model the bricks, the damaged plasticity model in Abaqus [50] is employed, which is developed based on the constitutive models proposed by Lubliner et al. [61] and Lee and Fenves [62] and can model the nonlinear compression hardening and tension stiffening behaviour of quasi-brittle materials [63]. It also includes consideration of stiffness degradation and recovery in repetitive compressive and tensile loading and is therefore suitable for applications where models are subjected to cyclic loading [57]. In addition to the material properties mentioned above, several other parameters are required to define the inelastic behaviour of damaged plasticity model, i.e., the dilation angle, the flow potential eccentricity, the ratio of initial equibiaxial compressive yield stress to initial uniaxial compressive yield stress (σ_{b0}/σ_{c0}), and the ratio of the second stress invariant on the tensile meridian to that on the compressive meridian (K_c). The yield surface and the flow potential are then calculated based on these parameters [61,62]. Due to the lack of test data, these parameters are referenced from Refs. [64–67]. The aforementioned data are summarised in Table 2.

Table 2
Material parameters for the damaged plasticity model of the brick material.

Uniaxial com-pressive strength (MPa)	Uniaxial tensile strength (MPa)	Density (kg/m^3)	Poisson's ratio	Young's modulus (MPa)	Dilation angle (°)	Flow potential eccentricity	σ_{b0}/σ_{c0}	K_c
20	2	2400	0.2	6700	30	0.1	1.16	0.6667

The stress-strain relationship used in the modelling is obtained by substituting the parameters of the brick material obtained from the material test into the formulae provided in the concrete design code [68]. The compressive stress-strain formula is presented as follows, where σ is the stress, ε is the strain, E is the elastic modulus, f_c is the uniaxial compressive strength, and ε_c is the corresponding compressive strain.

$$\begin{aligned}
&\sigma = (1-d_c)E\varepsilon \\
&d_c = \begin{cases} 1-\dfrac{\rho_c n}{n-1+x^n}, x \le 1 \\ 1-\dfrac{\rho_c}{\alpha_c(x-1)^2+x}, x > 1 \end{cases} \\
&x = \frac{\varepsilon}{\varepsilon_c}, \rho_c = \frac{f_c}{E\varepsilon_c}, n = \frac{E\varepsilon_c}{E\varepsilon_c - f_c}, \alpha_c = 0.157 f_c^{0.785} - 0.905
\end{aligned} \tag{1}$$

The tensile stress-strain relation is shown as follows:

$$\begin{aligned}
&\sigma = (1-d_t)E\varepsilon \\
&d_t = \begin{cases} 1-\rho_t\left[1.2-0.2x^5\right], x \le 1 \\ 1-\dfrac{\rho_t}{\alpha_t(x-1)^{1.7}+x}, x > 1 \end{cases} \\
&x = \frac{\varepsilon}{\varepsilon_t}, \rho_t = \frac{f_t}{E\varepsilon_t}, \alpha_t = 0.312 f_t^2
\end{aligned} \tag{2}$$

The damaged plasticity model includes both compressive and tensile damage variables (D_c and D_t) that increase with stress and strain. They characterise the degradation of elastic stiffness in compressive and tensile loading, respectively. The damage variable D at a given strain ε_1 can be calculated using the strain energy loss method described by Wang and Yu [69] and Qin and Zhao [70] according to Equation (3), where E_0 represents the original undamaged modulus of the material; $f(\varepsilon)$ represents the stress of the material, which is a function of its strain ε; $\int_0^{\varepsilon_1} f(\varepsilon)\mathrm{d}\varepsilon$ stands for the area between the stress-strain curve and the strain axis, i.e., the strain energy at the given strain ε_1; $\frac{1}{2}E_0{\varepsilon_1}^2$ represents the elastic strain energy, which is the hypothetical strain energy at the strain ε_1 if the material keeps elastic through the whole process.

$$D|_{\varepsilon=\varepsilon_1} = \frac{\frac{1}{2}E_0{\varepsilon_1}^2 - \int_0^{\varepsilon_1} f(\varepsilon)\mathrm{d}\varepsilon}{\frac{1}{2}E_0{\varepsilon_1}^2} \tag{3}$$

The degraded stiffness after compressive or tensile damage can hence be represented as Equation (4).

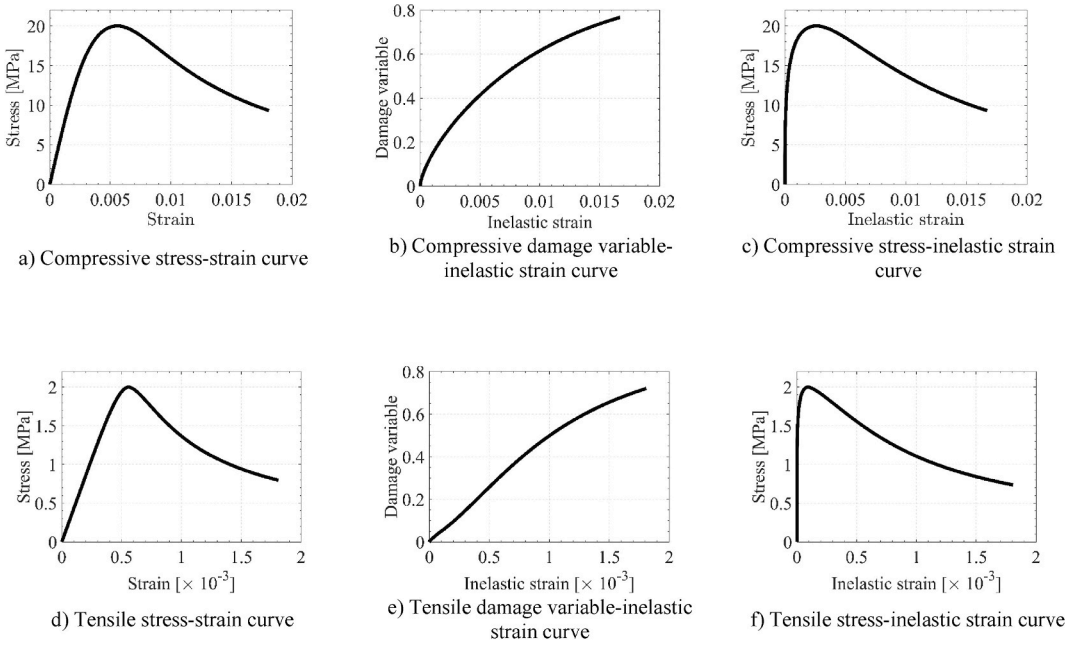

a) Compressive stress-strain curve
b) Compressive damage variable-inelastic strain curve
c) Compressive stress-inelastic strain curve
d) Tensile stress-strain curve
e) Tensile damage variable-inelastic strain curve
f) Tensile stress-inelastic strain curve

Fig. 7. Constitutive relationships of the brick material used in the model. a) Compressive stress-strain curve, b) Compressive damage variable-inelastic strain curve, c) Compressive stress-inelastic strain curve, d) Tensile stress-strain curve, e) Tensile damage variable-inelastic strain curve, f) Tensile stress-inelastic strain curve.

$$E = (1 - D_c \text{ or } D_t)E_0 \tag{4}$$

As mentioned above, D_c and D_t represent the stiffness degradation due to compressive and tensile damage, respectively. To comprehensively consider the influence of compressive and tensile damage on material stiffness, the stiffness degradation variable (SDEG, D_{ct}) is defined and calculated according to Equation (5) [57].

$$\begin{aligned} &1 - D_{ct} = (1 - s_t D_c)(1 - s_c D_t), s_t \geq 0, s_c \leq 1 \\ &s_t = 1 - w_t r^*, 0 \leq w_t \leq 1 \\ &s_c = 1 - w_c(1 - r^*), 0 \leq w_c \leq 1 \\ &r^* = \begin{cases} 1 \text{ if } \sigma_{11} > 0 \\ 0 \text{ if } \sigma_{11} < 0 \end{cases} \end{aligned} \tag{5}$$

where $\sigma_{11} > 0$ represents tension, while $\sigma_{11} < 0$ represents compression; w_c is the weight factor representing the recovery of stiffness degradation due to tensile damage when it changes from tension to compression; w_t represents the recovery of stiffness degradation due to compressive damage when it changes from compression to tension. In this study, the default values for these weight factors are used, i.e., $w_c = 1$ and $w_t = 0$, indicating that the stiffness degradation due to tensile damage is not manifested during the compressive stage (it takes effect again when the material status returns to tension), while the stiffness degradation due to compressive damage is inherited when the material status changes from compression to tension [57]. These values have been proven to be able to accurately simulate the behaviour of the interlocking brick material in previous studies [4,5,13,14,39]. As SDEG takes into account the damage of the material under complex stress conditions, it is used as an indicator of the damage status of the numerical models in the subsequent sections.

Based on Equations (1)–(3), the stress-strain relationships for the brick material under uniaxial compression and uniaxial tension, as well as the corresponding damage variables, can be determined. The inelastic strains are calculated in accordance with Equation (6) [57]. Fig. 7 illustrates the various constitutive relationships for the brick material used in the model. Specifically, the stress-inelastic strain relationships and damage variable-inelastic strain relationships under uniaxial compression (Fig. 7b and c) and under uniaxial tension (Fig. 7e and f) are input into Abaqus for defining the damaged plasticity constitutive model [50,57]. It is noted that in Abaqus, the inelastic strain under tension is referred to as “cracking strain”. For consistency in nomenclature between compressive and tensile behaviours, the term “inelastic strain” is uniformly adopted for both compressive and tensile constitutive relationships.

$$\varepsilon_{in} = \varepsilon - \frac{\sigma}{E_0} \tag{6}$$

For the reinforcement bars, a linear-plasticity constitutive model is adopted. The related parameters are taken from the paper by Menegon et al. [71], as shown in Table 3.

3.3. Contact

In conventional mortared masonry, bricks are bonded with mortar. In detailed numerical simulations, mortar layers are typically modelled explicitly, or interface elements are utilised [72]. In mortarless interlocking brick walls, no cohesion exists between individual bricks, which instead work in conjunction through direct normal and tangential contact. Therefore, the general contact algorithm in Abaqus is employed to simulate the contact amongst interlocking bricks. General contact is a surface-based contact algorithm, capable of automatically detecting contacting surfaces and imposing predefined contact properties [57]. This negates the need for specifying contact locations. The normal contact between interlocking bricks is modelled using the “hard contact” in Abaqus [57]. When two contact surfaces are compressed against each other, the hard contact algorithm allows pressure to transmit and minimises contact penetration; when the two contact surfaces separate, the acting force between them immediately becomes zero. The tangential contact between bricks is modelled using the Coulomb friction model. A friction coefficient of 0.7 is adopted, consistent with the friction coefficient value for masonry units sliding on each other when the contact interface is dry as specified in GB 50003-2011 [20]. This friction coefficient value also aligns closely with the coefficients used in previous studies on mortarless masonry [6,11,73]. Furthermore, since the four vertical reinforcing bars within the wall are ungrouted, contact may occur between the bars and surrounding bricks during in-plane cyclic loading. The normal contact between the reinforcing bars and bricks is also simulated using hard contact, while the tangential contact is modelled using the Coulomb friction model as well, with a friction coefficient of 0.57 [74]. It is worth noting that the reinforcing bars are also modelled using the first-order reduced-integration brick element C3D8R (the same element type as used for the bricks) to achieve better contact simulation results. Considering that smaller element sizes would significantly reduce the stable time increment and hence significantly increase computational time, the cross-section of the reinforcing bar is divided into 12 elements (Fig. 8), while a longitudinal element size of 17.5 mm is used. Such mesh sizes are proved to be fine enough for the study of overall response of the wall through convergence analyses. As can be seen in Fig. 8, the brick meshes around the

Table 3
Material parameters of reinforcing steel [71].

Density (kg/m^3)	Poisson’s ratio	Young’s modulus (MPa)	Yield strength (MPa)	Ultimate strength (MPa)	Ultimate strain
7850	0.3	200,000	550	660	0.095

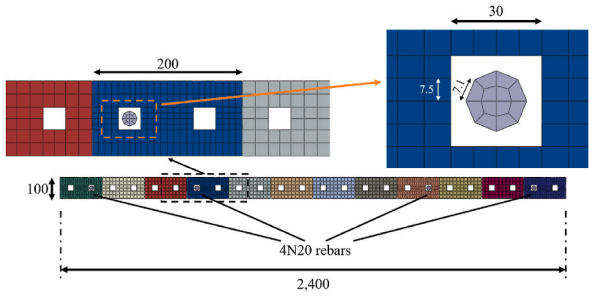

Fig. 8. Mesh of the cross section of the wall.

reinforcing bars are locally refined to avoid penetration during contact.

4. Model validation

Model validation is carried out through comparing the numerical simulation results with laboratory testing results.

4.1. Damage pattern

Fig. 9 compares the damage pattern of the interlocking brick wall in the lab test and that predicted by the numerical model. Initial cracking occurs at the right toe of the tested wall at a drift ratio of 1.9% (Fig. 9a). Similar toe damage is also observed in the numerical model at the same stage, as shown in Fig. 9b. At the drift ratio of 3.3% in the right direction, the test was terminated due to a plummet of the wall's lateral load bearing capacity from 120 kN to 43 kN (a drop of 64%) caused by the abrupt rupture of the leftmost rebar, leaving a diagonal-cracking-dominated failure pattern (Fig. 9c), which is also replicated by the numerical model (Fig. 9d).

4.2. Hysteresis response

Fig. 10 compares the hysteresis curves from both the laboratory test and the numerical simulation. A close match is observed between the two curves in the positive part, while some differences exist in the negative part due to the asymmetry of the test hysteresis curve. This is caused by the asymmetric damage of the tested wall owing to the brick imperfections. Such asymmetry, however, cannot be simulated in the perfect wall model. A more quantitative comparison is displayed in Table 4, where the lateral loads at each positive

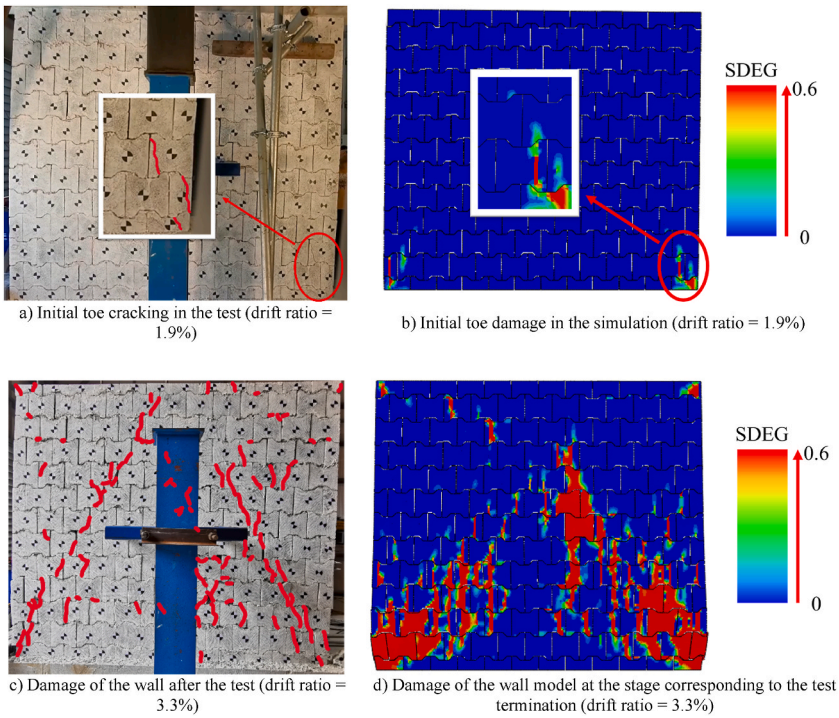

a) Initial toe cracking in the test (drift ratio = 1.9%)

b) Initial toe damage in the simulation (drift ratio = 1.9%)

c) Damage of the wall after the test (drift ratio = 3.3%)

d) Damage of the wall model at the stage corresponding to the test termination (drift ratio = 3.3%)

Fig. 9. Damage mode comparison of the interlocking brick wall. a) Initial toe cracking in the test (drift ratio = 1.9%), b) Initial toe damage in the simulation (drift ratio = 1.9%), c) Damage of the wall after the test (drift ratio = 3.3%), d) Damage of the wall model at the stage corresponding to the test termination (drift ratio = 3.3%).

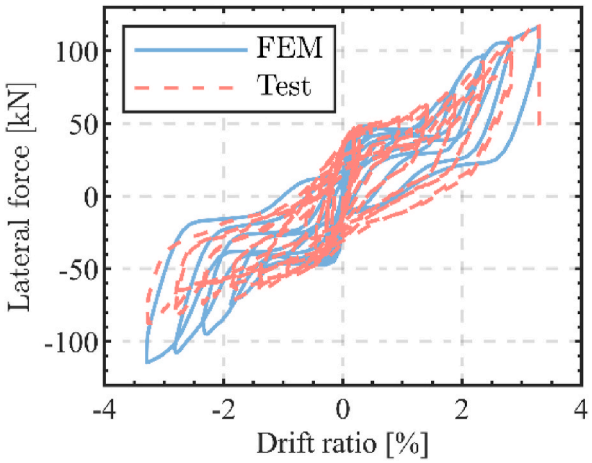

Fig. 10. Comparison of hysteresis curves of the interlocking brick wall.

Table 4
Comparison of lateral load and dissipated energy at each drift ratio between the test results and the simulation results.

Drift ratio	Lateral load			Dissipated energy		
	Test (kN)	Simulation (kN)	Error	Test (J)	Simulation (J)	Error
0.2%	44.7	41.9	−6.30%	299	110	−63.3%
0.3%	46.3	46.1	−0.40%	443	162	−63.5%
0.5%	47.4	46.7	−1.50%	711	512	−28.0%
0.9%	52.7	46.9	−11.00%	1341	1040	−22.5%
1.4%	63.8	57	−10.70%	2331	1902	−18.4%
1.9%	73.3	76.3	4.10%	3139	2617	−16.6%
2.4%	90.6	97.3	7.40%	3610	3505	−2.9%
2.8%	105.4	108.5	2.90%	4620	4588	−0.7%
3.3%	119.9	116.2	−3.10%	5478	5899	7.7%

drift ratio from the test and the simulation as well as their difference are presented. The average absolute error is 5.3%, with the largest discrepancy being 11% at the 0.9% drift ratio. The energy dissipation capabilities of the wall (i.e., the area enclosed by the hysteresis loop at various drift levels), as obtained from the numerical model and determined through the experiment, are also compared in Table 4. It is observed that when the drift ratio of the wall is below 0.5%, there is a substantial discrepancy between the test and simulation results in terms of energy dissipation. This can be attributed to the inevitable imperfections in the tested bricks due to manufacturing tolerances, which create pre-existing gaps in the test wall. When the wall lateral drifts are low, bricks in the test wall can move within these gaps and hence dissipate energy. The frictional energy dissipation caused by these pre-existing gaps cannot be reproduced in the simulation, where perfectly shaped bricks are modelled. Nonetheless, as the drift ratio grows, because of the mortarless design, inter-brick sliding initiates in areas without pre-existing gaps, which dissipates a significant amount of energy. Additionally, damage to the brick material develops and contributes substantially to energy dissipation as drifts increase, making the energy dissipated by damage surpass that by friction after the lateral drift ratio of 2.5%, as shown in Fig. 11. Consequently, the

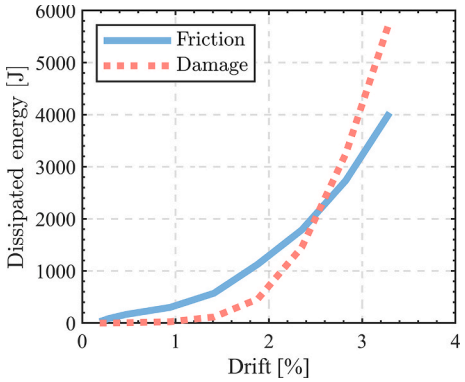

Fig. 11. Energy dissipated by friction and damage vs. lateral drift of the wall.

proportion of energy dissipation due to inter-brick sliding in pre-existing gaps becomes less significant compared to the total energy dissipation with increasing drift ratio. As a result, the energy dissipation values between the test and simulation get closer with the increase of the drift ratio of the wall. As shown in Table 4, at a drift ratio of 1.9%, the difference in energy dissipation between the test and simulation is around 15%. Furthermore, after 2.4% drift ratio, the discrepancies in the total dissipated energy between the test and simulation are within 10%.

Through the above comparison, it can be found that the developed numerical modelling approach is capable of providing reasonably accurate prediction of the response of mortarless interlocking brick wall under cyclic loading. This model will be used in the following sections for systematic investigations of the cyclic performance of the interlocking brick wall with different design parameters. It is worth noting that the developed model in this study presents better alignment with laboratory testing results compared to that in our previous study [39]. This is primarily because the reinforcement is modelled using the first-order reduced-integration brick element C3D8R with a finer mesh for surrounding bricks.

5. Results and analysis

Numerical simulations are firstly carried out to examine the influence of grouted and ungrouted vertical reinforcements in mortarless interlocking brick walls when subjected to cyclic loading. Then, the influence of wall-to-brick size ratio is also studied.

5.1. Influence of vertical reinforcement grouting method

For mortarless masonry structures, reinforcements can be ungrouted to improve construction efficiency; while for conventional masonry structures, reinforcements are mostly grouted [75]. To study the influence of the reinforcement grouting methods on the hysteretic behaviour of mortarless interlocking brick walls, two numerical models are generated, where wall B1 has ungrouted reinforcement, while B2 has reinforcements grouted with the bricks. It is noted that the brick holes without vertical reinforcement are not grouted, making the wall a partially grouted wall. The brick and reinforcement materials are the same as in the validated model as described in Section 3.2. The rest of the parameters are listed in Table 5. To simplify the analysis, the material parameters of the grout are set to be the same as those for the brick material with C3D8R elements. No slippage between reinforcements and surrounding grout is considered with the embedded-region constraint applied [57]. The bonding between the grout and the surrounding bricks is realised through the cohesive contact with parameters in reference to Abdulla et al. [76]. Table 6 and Fig. 12 show the numerical simulation results. Following Matsumura [77] and Calderón et al. [78], the peak average shear stress in this study is calculated as the ratio of the peak lateral load resisted by the wall to the gross cross-section area of the wall. The drift capacity in this study refers to the lateral drift at which the post-peak lateral load resisted by the wall drops to 80% of the peak value, i.e., the near-collapse (NC) limit state prescribed in EC8-Part 3 [79]. The equivalent damping ratios listed in Table 6 and following sections are the average equivalent damping ratios between the time when the pre-peak lateral load rises to 80% of the peak load and the instance when the post-peak lateral load drops to 80% of the peak. Such a range is chosen because it is essential to quantify the equivalent damping ratios when the wall is approaching its limit state to adequately reflect the energy dissipation capacity of the wall, while the amount of dissipated energy is limited when the wall is still in the elastic stage regardless of the damping ratio.

It is seen that compared to B1, wall B2 has a higher strength but a lower ductility. Specifically, the peak strength of B2 reaches 0.671 MPa, which is 40% higher than that of B1 (0.48 MPa), while the drift capacity is only 3.97%, which is 34% lower than that of B1. This is because in the grouted wall B2, the relative movement between bricks is partly hindered by the grout. Fig. 13 shows the vertical displacement contour of B1 and B2 at a drift ratio of 2.35%, where U2 is the vertical displacement. It can be seen that B1 exhibits a flexural bending response, resulting in a gradual increase in the vertical displacement from left to right. Because the wall has no tensile strength from mortarless bricks, horizontal gaps can be seen between different brick courses under the flexural bending moment. In contrast, from Fig. 13b it can be seen that when the rebars are grouted, under the same drift ratio, the vertical displacement distribution of the wall no longer shows a clear decrease from right to left; the vertical displacements of the bricks in the tensile side are significantly lower than those at the corresponding positions in B1. This is because after the vertical rebars are grouted, there is obvious bonding and friction between the grout and the surrounding bricks, which restricts the separation of the bricks in the vertical direction. Therefore, in B2, the shear keys of the bricks are more tightly interlocked. Meanwhile, significant differences are observed in the deformation patterns and the magnitude as well as the distribution of stress in the reinforcing bars between B1 and B2. Fig. 14a and b respectively show the Mises stress in the rebars at 2.35% drift ratio. As shown in Fig. 14a, the distribution of lateral displacement in the rebars of B1 is relatively uniform exhibiting no apparent bending or shear deformation. On the other hand, Fig. 14b reveals a more complex lateral deformation pattern in the rebars of B2, with all four rebars displaying noticeable bending or shear deformation. In terms of stress, a relatively uniformly distributed stress is observed across the rebars in B1. Localised rebar yielding (denoted by the grey area on the rebars) occurs only at the end of the outermost rebar on the tensile side, with the maximum stress at this point reaching only 557.9 MPa. The stress in the two rebars on the compressive side is close to zero, indicating that these rebars are virtually unaffected. In contrast, B2 exhibits a more uneven stress distribution across all rebars corresponding to the complex deformation patterns

Table 5
Design parameters of interlocking brick wall with different rebar grouting conditions.

No.	Rebar grouting	Wall length (mm)	Wall height (mm)	Shear span (mm)	Wall thickness (mm)	Axial precom-pression (MPa)	Vertical reinforce-ment	Reinforce-ment ratio
B1	Ungrouted	2400	2125	2500	100	0.47	4ø20	0.5%
B2	Grouted							

Table 6
Simulation results of interlocking brick wall with different rebar grouting conditions.

No.	Peak lateral force (kN)	Peak average shear stress (MPa)	Drift capacity	Average equivalent damping ratio around the peak strength
B1	115.33	0.480	5.98%	12.53%
B2	160.98	0.671	3.97%	14.38%

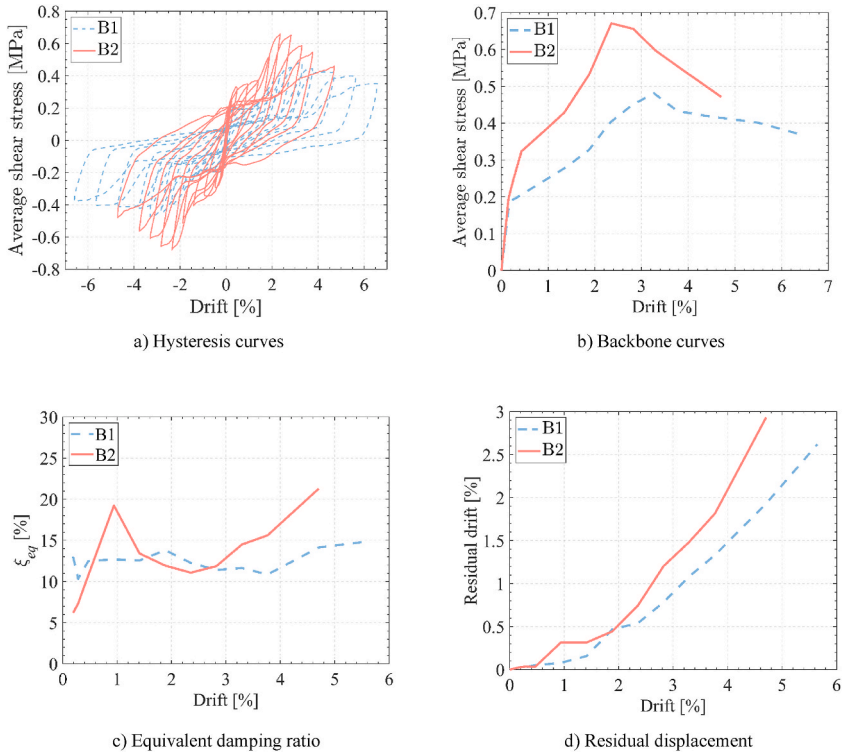

Fig. 12. Simulation results of interlocking brick wall with different rebar grouting conditions. a) Hysteresis curves, b) Backbone curves, c) Equivalent damping ratio, d) Residual displacement.

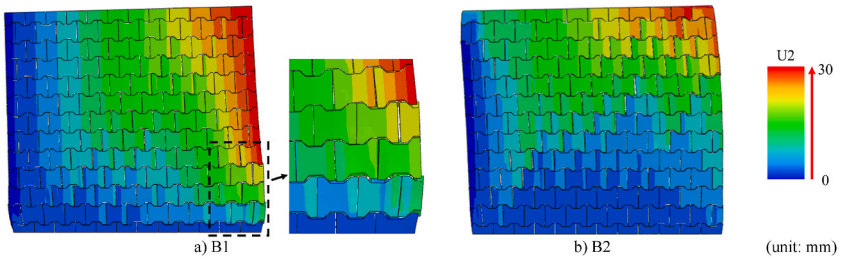

Fig. 13. Vertical displacement distribution of interlocking brick walls with different rebar grouting conditions (drift ratio = 2.35%, deformation scale factor = 2). a) B1, b) B2, (unit: mm).

described above. Noticeable yielding occurs in the outermost rebar on the tensile side, with a maximum stress (606 MPa) significantly exceeding the yield strength. Non-negligible stress is also observed in the rebars on the compressive side, reflecting the mutual confinement between the rebars and the surrounding grout and bricks. Overall, in the grouted wall (B2), the material strengths of both the bricks and the rebars are more fully utilised, making the grouted wall stronger but also causing more material damage and hence a lower ductility. Regarding the energy dissipation performance, the significantly higher strength of B2 leads to more severe brick damage and hence increases its energy dissipation. Therefore, the equivalent damping ratio of B2 is generally higher than that of B1. It is noted that at a drift ratio of 0.94%, the equivalent damping ratio of B2 exhibits a spike (an equivalent damping ratio of 19.24%). This is caused by the failure of the bonding between the grout and the surrounding bricks. Afterwards, the equivalent damping ratio of B2 increases rapidly and surpasses 20% when the drift ratio reaches 4.5%, indicating the rapid development of wall damage in B2. The

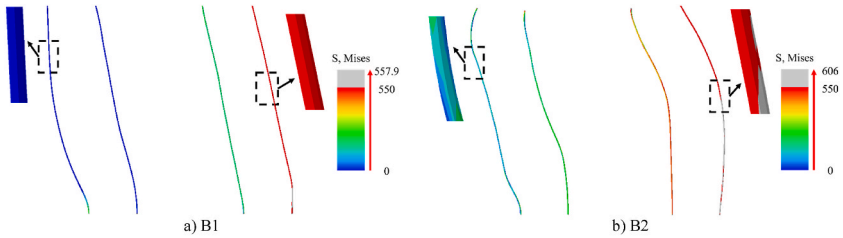

Fig. 14. Rebar stress of interlocking brick walls with different rebar grouting conditions (drift ratio = 2.35%, deformation scale factor = 10) (unit: MPa). a) B1, b) B2.

more severe material damage in B2 also significantly increases its residual displacement. When B2 reaches its peak lateral strength (at 2.35% drift ratio), its residual deformation reaches 15.9 mm (a residual drift ratio of 0.75%), which is 38% higher than that of B1 (11.49 mm, i.e., a residual drift ratio of 0.54%). Afterwards, the strength of B2 starts to degrade rapidly; thus, the difference between the residual displacements of the two walls is further amplified.

Overall, for the studied mortarless interlocking brick walls, grouting vertical reinforcements improves the lateral strength of the walls. However, walls with unbonded reinforcements outperform in terms of deformability and residual deformation. In consequence, in the following sections, the primary focus is the performance of mortarless interlocking brick walls with unbonded reinforcements.

5.2. *Investigation of wall-to-brick size ratio*

Previous studies [24,80] found that wall-to-brick size ratio could influence the failure mode of conventional masonry walls subjected to in-plane cyclic loading. To examine its influence on mortarless interlocking brick walls, numerical simulation is carried out on three interlocking brick walls (S1, S2 and S3) with their details tabulated in Table 7. Since it is difficult to quickly alter brick size in production in possible subsequent validation tests [81], in the simulations, the brick size remains constant while the walls have different sizes but the shear span ratio (the ratio of shear span to wall height [23,24]) and the aspect ratio of the walls are kept the same. Such a numerical modelling strategy to investigate the influence of wall-to-brick size ratio is also adopted by Dolatshahi et al. [24]. The brick-to-size ratio is then quantified by the ratio of the height of the wall to the height of a single brick. The simulation results are summarised in Table 8 and Fig. 15.

Fig. 15a and b show the hysteresis curves and the backbone curves. It can be seen that with the largest relative brick size (the smallest wall size), S1 reaches its peak lateral strength the earliest at 2.33% drift ratio, but with the highest peak average shear stress (0.509 MPa). The strength of S1 drops to 80% of the peak value at a drift ratio of 5.08%, indicating the loss of the load-carrying capacity. In contrast, with smaller relative brick sizes, walls S2 and S3 exhibit lower strength and better ductility. S2 reaches its peak strength of 0.48 MPa at a drift ratio of 3.29% and its strength drops to 80% of the peak value at a drift ratio of 5.98%. Although S3 reaches its peak strength (0.417 MPa) at a drift ratio of only 2.36%, its post-peak strength degrades more gradually, and it does not drop to 80% of the peak strength until 5.06% drift ratio.

The above different performances of the three walls are primarily due to the difference in the relative size of bricks. Fig. 16 illustrates the distribution of the minimum principal stress of three walls at their maximum lateral strengths. It is evident that there are multiple compressive struts extending from the bottom right corner to the upper left of the wall. It is noteworthy that due to the geometric shape of the bricks, within each brick, the width, location and angle of the strut are relatively fixed, originating from the small key at the bottom right corner and the adjacent groove area, extending to the small key at the top left corner and the groove area to its right, as illustrated in the shaded area of Fig. 17. Thus, the compressive struts in the wall are discontinuous, and the width of each strut is approximately equal. As the wall to brick size ratio increases, the compressive struts become more dispersed, and the number of struts does not grow proportionally with the size ratio increment. From Fig. 16a, it can be found that in wall S1 there are two struts that transverse the entire wall diagonally. In S2 and S3, the relative brick size is smaller, which impacts the efficiency of load transfer and hence the distribution of compressive struts. As seen in Fig. 16b, wall S2 has three prominent struts, of which only two transverse the entire wall. Fig. 16c shows wall S3 has five struts, yet the width and the stress borne by each strut are not equal, indicating that not all struts are fully utilised in terms of load-bearing capacity. Therefore, with an increase of the wall to brick size ratio, the ratio of the diagonal bearing area to the wall's cross-sectional area decreases, leading to a reduced material efficiency and a reduction in the lateral strength of the wall.

Under the same lateral drift ratio, the contribution of material deformation to the total lateral deformation in S1 is greater than that in S2 and S3, which can be discerned from the frictional and material damage energy dissipation of each wall. This is because, under cyclic loading, inter-brick movements lead to significant energy dissipation through friction [13,14]; meanwhile, bricks tend to experience plastic deformation and damage, and thus also consume energy. Therefore, the contribution of material deformation and inter-brick movement to the overall deformation of the wall can be judged from the ratio of energy dissipated by material plastic deformation and damage (E_p) to energy dissipated by friction (E_f) [13]. Fig. 18 presents the variation of material damage energy dissipation to friction energy dissipation in walls S1–S3 against the lateral drift ratio. Up to a drift ratio of 4.6%, wall S1 has a greater ratio than those in S2 and S3, indicating more material damage in S1 due to more significant material deformation. Therefore, S1 reaches its peak strength earliest resulting in the lowest drift capacity, large residual drifts at high drift ratios, and the highest equivalent damping ratio around the peak strength (Fig. 15b-d). It is worth noting that both the strength and drift capacity of S3 are lower than S2 and both the equivalent damping ratio and the residual drift of S3 increase rapidly at large drift ratios, being the highest

Table 7
Design parameters of interlocking brick wall with different sizes.

No.	Inter-locking brick height (mm)	Wall length (mm)	Wall height (mm)	Wall thick-ness (mm)	Shear span (mm)	Aspect ratio (length to height)	Shear span ratio (length to shear span)	Wall-to-brick height ratio	Axial precom-pression (MPa)	Vertical reinfor-cement	Reinfor-cement ratio	Number of contact inter-faces	Total contact area (mm^2)
S1	205	1200	1075	100	1250	1.12	0.96	5.24	0.47	2∅20	0.5%	908	1,370,458
S2		2400	2125		2500	1.13		10.37		4∅20		2453	5,564,333
S3		3600	3175		3750	1.13		15.49		6∅20		5516	12,579,124

Table 8
Simulation results of interlocking brick wall with different sizes.

No.	Peak lateral force (kN)	Peak average shear stress (MPa)	Drift capacity	Average equivalent damping ratio around the peak strength
S1	73.25	0.509	5.08%	14.08%
S2	115.33	0.480	5.98%	12.53%
S3	150.23	0.417	5.06%	12.36%

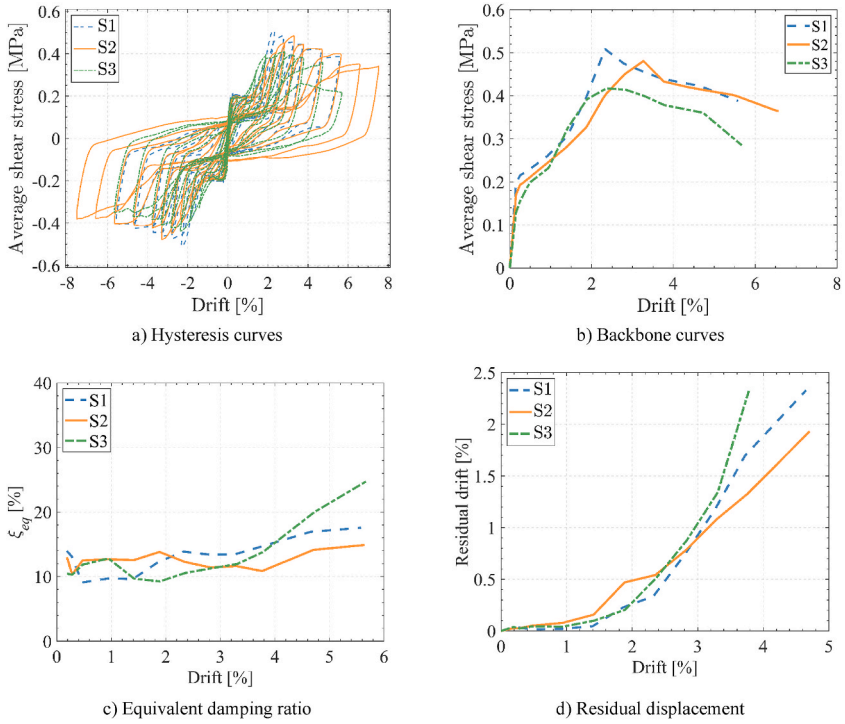

Fig. 15. Simulation results of interlocking brick wall with different sizes. a) Hysteresis curves, b) Backbone curves, c) Equivalent damping ratio, d) Residual displacement.

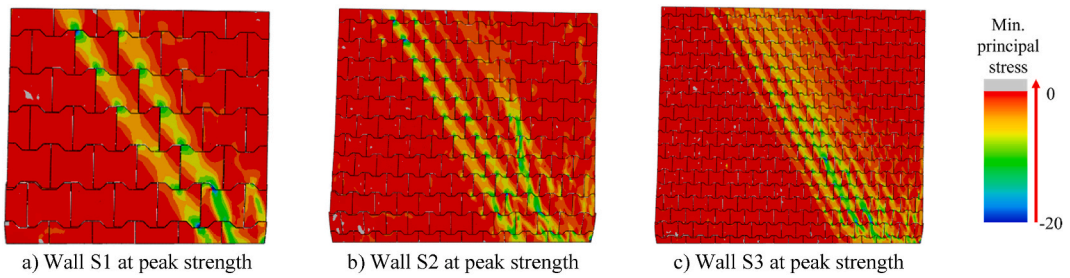

Fig. 16. The distributions of minimum principal stress at the peak lateral strength of walls S1–S3. a) Wall S1 at peak strength, b) Wall S2 at peak strength, c) Wall S3 at peak strength.

among those of the three walls (Fig. 15c and d). This is because, as shown in Table 7, wall S3 has a larger height-to-thickness ratio (31.75) than S2 (21.25). As shown in Figs. 1b, c and 2d, e, the studied interlocking brick is asymmetric in the front and back surfaces. When the ratio of wall height to thickness is too large, under the combined action of axial precompression and cyclic loading, the wall is prone to buckle as drift ratio increases. Since out-of-plane responses are not the focus of this paper, it is not explicitly discussed herein.

6. Parametric study

The influence of various design parameters (such as the level of axial precompression, shear span ratio of the wall, etc.) on the

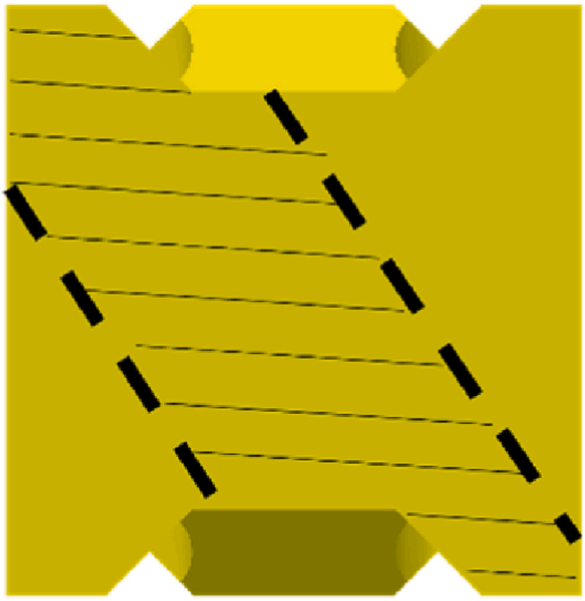

Fig. 17. The typical compressive strut in an interlocking brick.

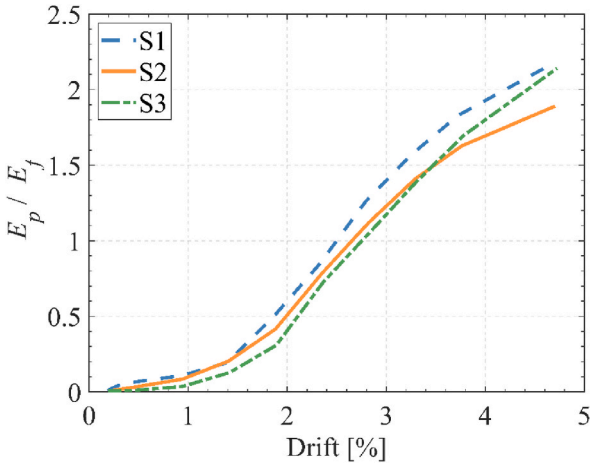

Fig. 18. Ratio of cumulative energy dissipated by different mechanisms (E_p: energy dissipated by material damage; E_f: energy dissipated by friction).

performance of conventional mortar-bonded masonry walls has been widely studied and summarised [18,19,23,78,82–88]. However, research on the impact of changes in these parameters on the performance of mortarless interlocking brick walls remains scarce. In this section, numerical simulation is performed to conduct parametric studies on the response of mortarless interlocking brick walls under cyclic loading. The influences of axial precompressions, shear span ratios and friction coefficients on the performance of interlocking brick walls including lateral load-bearing capacity, ductility, and energy dissipation capability are investigated.

Table 9
Design parameters of the interlocking brick walls under varying axial precompressions.

No.	Wall length (mm)	Wall height (mm)	Shear span (mm)	Wall thickness (mm)	Axial precompression (MPa)	Axial precompression ratio	Vertical reinforcement	Reinforcement ratio
P1	2400	2125	2500	100	0.235	2.90%	4ø20	0.5%
P2					0.3525	4.35%		
P3					0.47	5.80%		
P4					0.5875	7.25%		
P5					0.705	8.70%		

6.1. Influence of axial precompression

Previous studies demonstrated that a higher axial precompression level influences the ductility and lateral strength of conventional masonry walls [23,82]. A higher axial precompression tightens the interlocking between aggregates, reduces the width of cracks and widens the compressive struts in the diagonal direction of the wall, which ultimately increase the lateral strength of masonry walls [16,24]. For mortar-less interlocking brick walls, more considerable interlocking could be provided by the relatively large keys and the mortar-less construction method. Therefore, the influence of axial precompression on interlocking brick walls may differ from that on conventional masonry walls. To quantify the influence, a group of numerical simulations is performed on mortarless interlocking brick wall models whose geometric dimensions remain unchanged (the length $L = 2400$ mm; the height $H = 2125$ mm; the thickness $T = 100$ mm; the shear span $H_0 = 2500$ mm) while the axial load N applied on the top reference point (Fig. 4) is varied so that the axial precompressions p applied on the wall vary between 0.235 MPa and 0.705 MPa. Detailed parameters are listed in Table 9. The brick material and the reinforcement material remain the same as in the validated model as described in Section 3.2. The axial precompression ratio is defined as the ratio of the axial precompression to the prism compressive strength of the mortarless interlocking bricks; the prism compressive strength of the studied mortarless interlocking bricks is calculated using the formula proposed by Shi et al. [4], yielding a result of 8.1 MPa for the bricks made of the material described in Section 3.2.

The simulation results are summarised in Table 10 and Fig. 19. The hysteresis curves of the interlocking brick wall under different axial precompressions are presented in Fig. 19a, where the ordinate is the average cross-section shear stress of the wall, i.e., the ratio of the total lateral force to the gross cross-section area of the wall, while the abscissa is the drift ratio of the wall, namely the ratio of the lateral deformation on top of the wall to the wall height.

From Table 10 and Fig. 19b, it can be observed that the lateral strength of the mortarless interlocking brick wall increases with the increase of axial precompression. The linear regression analysis in Fig. 19b has an R-squared value of 0.9845, indicating a high degree of fit and an approximate linear relationship between the wall's lateral strength and the axial precompression. This is because the lateral strength of the mortarless interlocking brick wall is primarily provided by the shear strength of interlocking keys and the friction between the bricks, both of which increase approximately linearly with axial precompression [5]. On the other hand, it can also be found that with the increase of axial precompression, the drift capacity of the wall decreases approximately linearly (R-squared value = 0.9467), indicating the reduction in the ductility of the mortarless interlocking brick wall is also proportional to the axial precompression. This is because a larger axial compressive stress and the subsequent larger lateral force resisted by the interlocking brick wall induces wider diagonal compressive struts and larger plastic strain areas near the wall toes under the same lateral drift, as shown in Fig. 20. The more severe damage to the brick material leads to the lower ductility of the wall when subjected to a higher axial precompression. On the other hand, both the rigid body movement of the wall (rocking response) and the inter-brick sliding become less significant when the wall is subjected to higher axial precompressions, which results in more significant material damage on the wall at smaller drift ratios. Similar to the trend of peak average shear stress, according to Table 10 and Fig. 19d, the average equivalent damping ratio around the peak load increases approximately linearly with the increase of axial precompression (R-squared value = 0.9219). This is also primarily attributed to the more pronounced plastic deformation and material damage in the wall caused by the higher axial precompression.

6.2. Influence of shear span ratio

In the context of walls, the shear span ratio is defined as the quotient of the distance from the base of the wall to the inflection point where the concentrated lateral force is applied (H_0), and the wall's length in the direction of shear (L) [23,24,54]. Within masonry design standards, this ratio is commonly expressed as $M/(Vd)$, where M represents the bending moment on the wall in the direction of shear, V denotes the horizontal shear force within the range from the base of the wall to the point of lateral force application, and d refers to the length of the wall in the direction of shear [18,19,84,85]. In the design of conventional masonry walls, the shear span ratio is an important parameter, which has direct influences on the lateral strength and the drift capacity of walls [18,24]. For the mortarless interlocking brick wall, the rocking of the wall as well as the rocking of local bricks is an important response characteristic under in-plane lateral loads [13,14,39]. The change in shear span ratio may affect the rocking behaviour of the wall and potentially differentiate the impact of shear span ratio on the mortarless interlocking brick wall from that on conventional masonry walls. To investigate the effect of shear span ratio, five mortarless interlocking brick wall models are established with equal heights ($H = 2125$ mm), equal shear span ($H_0 = 2500$ mm) and equal thicknesses ($T = 100$ mm) but different lengths (L) of 1200 mm, 1800 mm, 2400 mm, 3000 mm, and 3600 mm, respectively. The axial load N applied at the top of the wall is varied according to the cross-section area of the wall to ensure that the axial precompression p on each wall remains at 0.47 MPa. The vertical reinforcement is also adjusted to ensure a reinforcement ratio of 0.5% in all the walls. Table 11 summarises the model parameters. It is important to note that in Table 11, the shear span ratio is calculated as the quotient of the wall's length in the direction of shear to the shear span. This is because

Table 10
Simulation results of the interlocking brick walls under varying axial precompressions.

No.	Peak lateral force (kN)	Peak average shear stress (MPa)	Drift capacity	Average equivalent damping ratio around the peak load
P1	96.92	0.404	7.49%	9.41%
P2	105.50	0.439	6.46%	11.91%
P3	115.33	0.480	5.98%	12.53%
P4	124.29	0.518	3.90%	13.65%
P5	128.49	0.535	3.62%	14.27%

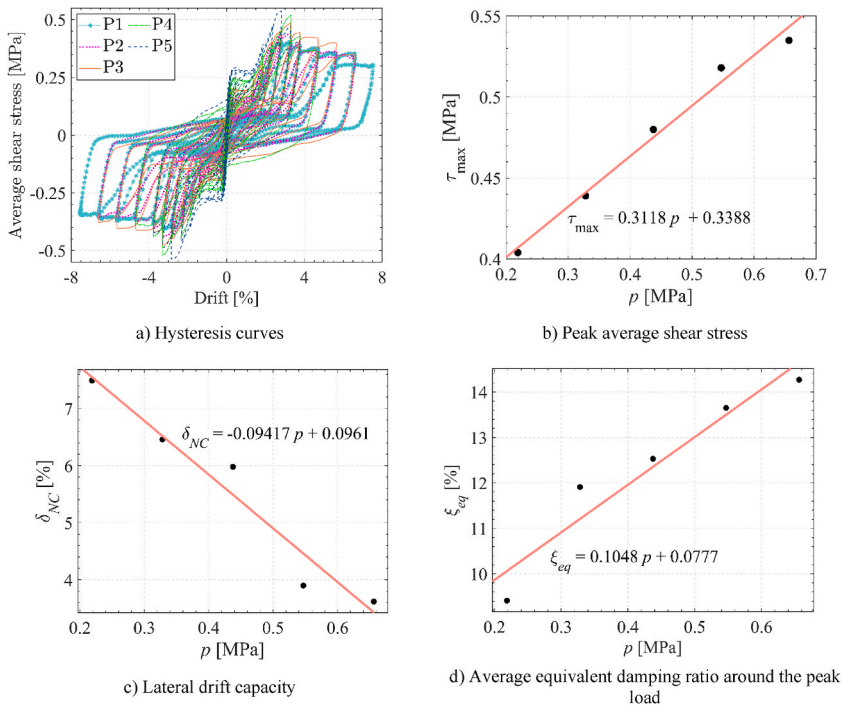

Fig. 19. Simulation results of interlocking brick wall under various axial precompressions. a) Hysteresis curves, b) Peak average shear stress, c) Lateral drift capacity, d) Average equivalent damping ratio around the peak load.

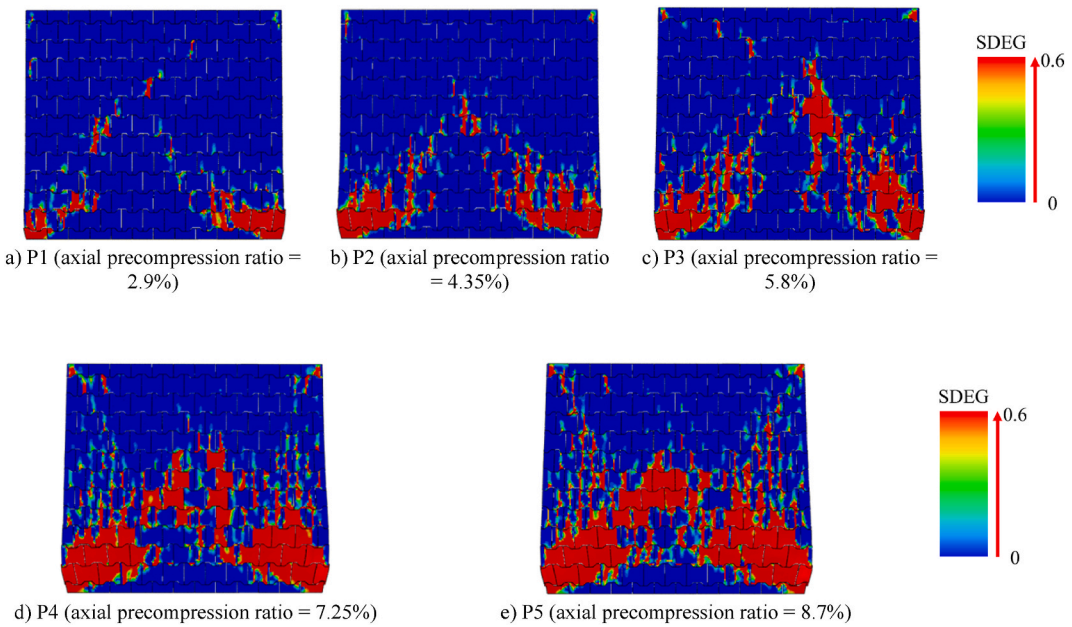

Fig. 20. Damage of the walls under different axial precompression ratios after the loop of 3.3% drift ratio. a) P1 (axial precompression ratio = 2.9%), b) P2 (axial precompression ratio = 4.35%), c) P3 (axial precompression ratio = 5.8%), d) P4 (axial precompression ratio = 7.25%), e) P5 (axial precompression ratio = 8.7%).

in this study, the height of the wall and the shear span are constants; the variation in the shear span ratio among the walls is a result of differing lengths of those walls in the shear direction. For simplicity, the wall's length in the direction of shear is used as the numerator and the shear span as the denominator in the computation of the shear span ratio. The simulation results are shown in Table 12 and Fig. 21.

Fig. 21a shows the hysteresis curves of the interlocking brick walls with different shear span ratios. It can be seen that the hysteresis

Table 11
Design parameters of interlocking brick wall with varying shear span ratios.

No.	Wall length (mm)	Wall height (mm)	Shear span (mm)	Wall thickness (mm)	Shear span ratio (length to shear span)	Axial precompression (MPa)	Vertical reinforcement	Reinforcement ratio
L1	1200	2125	2500	100	0.48	0.47 MPa	2ø20	0.5%
L2	1800				0.72		2ø24	
L3	2400				0.96		4ø20	
L4	3000				1.2		4ø22	
L5	3600				1.44		6ø20	

Table 12
Simulation results of interlocking brick wall with varying shear span ratios.

No.	Peak lateral force (kN)	Peak average shear stress (MPa)	Drift capacity	Average equivalent damping ratio around the peak load
L1	33.17	0.276	10.14%	10.42%
L2	72.35	0.402	5.44%	11.99%
L3	115.33	0.480	5.98%	12.53%
L4	156.18	0.521	5.25%	13.75%
L5	198.71	0.552	5.61%	15.73%

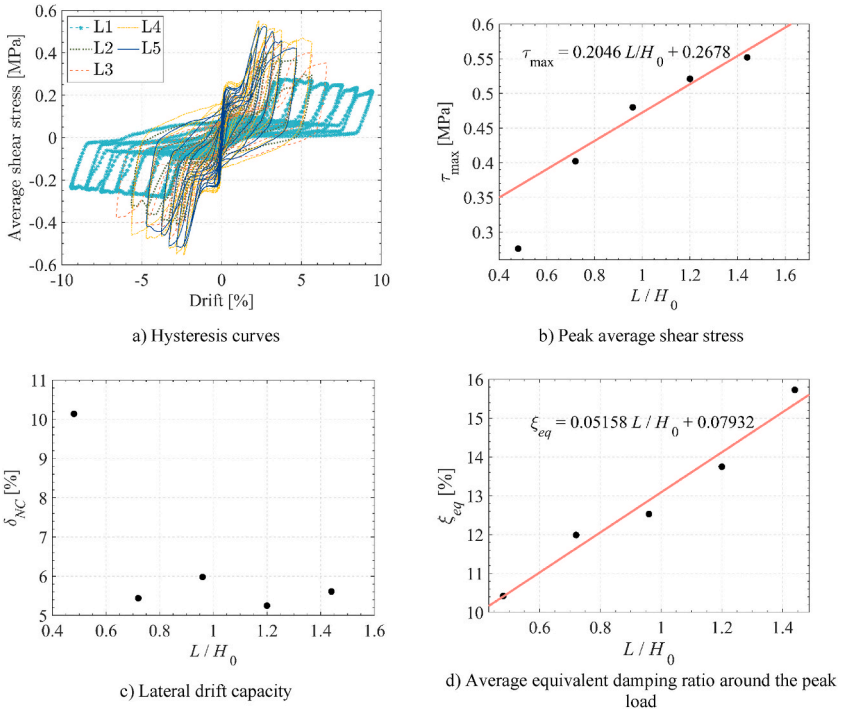

Fig. 21. Simulation results of interlocking brick wall with various shear span ratios. a) Hysteresis curves, b) Peak average shear stress, c) Lateral drift capacity, d) Average equivalent damping ratio around the peak load.

curves of wall L1 are significantly narrower than the others, while those of L2 to L5 are plumper. It can be inferred that the wall L1 (with a shear span ratio of 0.48) is primarily subjected to flexural failure, while the walls L2 to L5 primarily exhibit shear failure [83]. This can also be observed in Fig. 22, which shows the damage to the walls when they reach their maximum lateral drift capacity (i.e., when the load drops to 80% of their lateral load-bearing capacities). Despite the severe damage and crushing to the bricks at the toes of L1, it does not develop diagonally upwards, and the upper half of the wall experiences very minor damage. In contrast, the damages in walls L2 to L5 develop along the diagonal direction, resulting in significant damage in the middle and upper parts of the walls. Typically, damage is formed around the two top corners of the wall in L2 to L5 but not in L1. The difference in the failure mode between L1 and the others explains the significant differences in maximum shear stress and the drift capacity between L1 and the other walls in Fig. 21b and c.

Fig. 21b correlates the lateral strength and the shear span ratio. It can be seen that the lateral strength of L1 with a shear span ratio

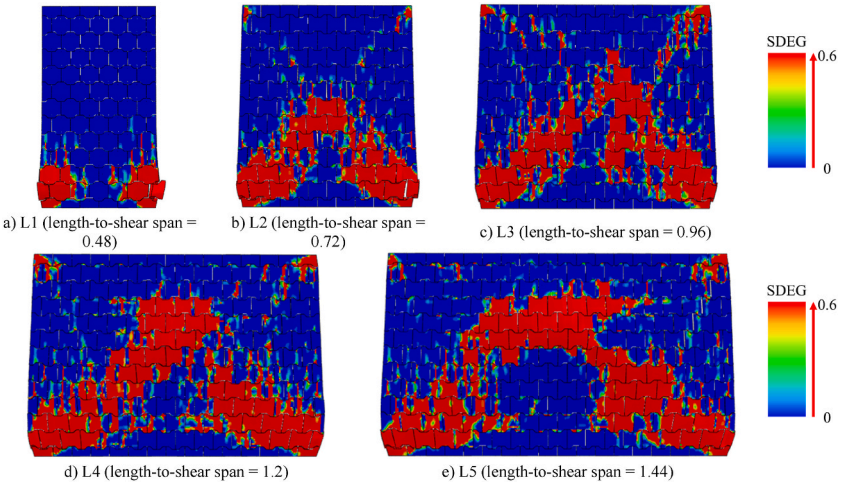

Fig. 22. Damage after strength degrading to 80% peak strength for walls with varying shear span ratios. a) L1 (length-to-shear span = 0.48), b) L2 (length-to-shear span = 0.72), c) L3 (length-to-shear span = 0.96), d) L4 (length-to-shear span = 1.2), e) L5 (length-to-shear span = 1.44).

of 0.48 is only 0.276 MPa, which is significantly lower than the others. The lateral strengths of L2 to L5 increase approximately linearly with the increase of shear span ratio (R-squared value = 0.9534). This is because the shear capacity of mortarless interlocking brick walls mainly depends on the interlocking between shear keys. When the contact between shear keys is tighter, the shear capacity of the shear keys can be more fully utilised. However, due to the lack of vertical constraint, the mortarless interlocking brick walls tend to experience rocking response under lateral loads [13,14,39], which weakens the contact between the shear keys of adjacent brick layers. Take wall L2 as an example (Fig. 23a). The rocking response is developed at a lateral drift of 2.8%, leading to the separation between the shear keys of the upper and lower layers near the lower left corner of the wall. To quantify this separation, the uplifting angle in the vertical direction is calculated, defined as in Equation (7).

$$\theta_{uplift} = \frac{\left| u_{A,vertical} - u_{B,vertical} \right|}{l_{AB,undeformed}} \tag{7}$$

where θ_{uplift} is the uplifting angle of the wall, $u_{A,vertical}$ is the vertical displacement of point A in Fig. 23a, $u_{B,vertical}$ is the vertical displacement of point B in Fig. 23a, and $l_{AB,undeformed}$ is the distance between points A and B before any loading is applied (Note that points A and B are at the same height before loading). In other words, the uplifting angle, as depicted in Fig. 23a, corresponds to the angle formed between lines AB and CD. Fig. 23b shows the uplifting angle of walls with different shear span ratios at different drift ratios. It can be seen that as the shear span ratio increases, the uplifting angle of the wall at each drift ratio becomes smaller. Therefore, the contact between the shear keys of adjacent layers of bricks in walls with larger shear span ratios is tighter, which enables the shear keys to be more fully utilised, resulting in an increase in the average peak shear stress of the wall as the shear span ratio increases.

Table 12 and Fig. 21c summarise the lateral drift capacities of the modelled interlocking brick walls. It can be seen that the lateral drift capacity of L1 is significantly larger than the others (over 10%). This is because L1 mainly fails in flexural failure mode, while L2 to L5 mainly fail with diagonal shear failure (Fig. 22), and the drift capacity of a wall failing in flexural mode is significantly larger than that of a wall failing in diagonal shear mode [83]. The lateral drift capacity of all other interlocking brick walls (except L1) is between 5% and 6%. This reflects that the drift capacity of mortarless interlocking brick walls in shear failure mode is not sensitive to the shear

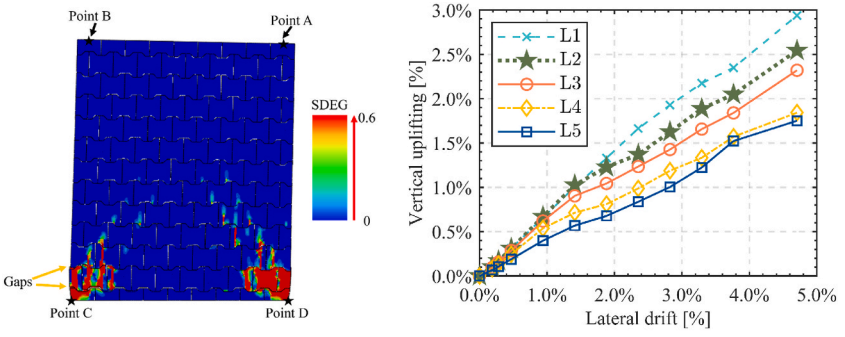

Fig. 23. Uplifting of the walls with different shear span ratios. a) Uplifting of L2 at 2.8% lateral drift, b) Uplifting angle of line AB at each drift level.

span ratio of the wall, which is similar to the observation in conventional masonry walls [23]. Nevertheless, in Fig. 21d which shows the averaged equivalent damping ratio of the walls with different shear span ratios, it can be seen that the average equivalent damping ratio before the failure of the mortarless interlocking brick walls approximately increases linearly with the shear span ratio (R-squared value = 0.9672). This is because with the increase of shear span ratio, the contact between the shear keys of the interlocking bricks becomes tighter (Fig. 23b) and the corresponding frictional energy dissipation increases, resulting in an increase in the equivalent damping ratio.

6.3. Influence of friction coefficient

When subjected to in-plane cyclic loading, mortarless interlocking brick wall exhibits repetitive relative sliding between adjacent bricks [39]. To examine the influence of friction coefficient at brick interface on the wall behaviour, a series of numerical simulations is conducted on interlocking brick walls with different friction coefficients. Model details are tabulated in Table 13, where the lower bound of the friction coefficient is 0.3 representing the friction coefficient between damp masonry stipulated by the Chinese Masonry Structure Design Code [20], and the upper limit is 1.0, as stipulated by the Canadian Masonry Structure Design Code [17], indicative of the friction coefficient between masonry and roughened concrete. It is pertinent to highlight that most existing studies adopted friction coefficients within this specified range [6,11,73,89–93]. As in previous sections, the material properties assigned to both the brick and reinforcement materials remain consistent with those detailed in Section 3.2.

Table 14 and Fig. 24 show the numerical simulation results. Fig. 25a illustrates the hysteresis curves of the walls with different friction coefficients, where the peak strengths are reasonably similar. Consequently, as shown in Fig. 24b, the peak average shear stress of the walls differs minimally, with the largest peak average shear stress (belonging to walls F2 and F3) being only 3.4% greater than the smallest (belonging to wall F1). It demonstrates that friction coefficient has negligible influence on the peak lateral strength of mortarless interlocking brick walls. This is because the interlocking keys constrain the bricks in the in-plane direction, making the lateral strength of the wall primarily governed by the strength of brick material rather than the friction between bricks, as observed by Sturm et al. [6].

The hysteresis curves of the walls exhibit variations after peak strength as depicted in Fig. 24a, indicating different strength degradation behaviours for interlocking brick walls with varying friction coefficients. This is because under the same axial pre-compression, higher friction coefficients between the bricks result in less displacement contributed by the relative sliding between bricks. It leads to more displacement contributed by brick deformation, and thus more severe damage. Fig. 25 displays the damage contours of these four walls at a drift ratio of 5.7%, showing that higher friction coefficients correspond with more severe and widespread damage, thus indicating a relatively lower drift capacity for walls with higher friction coefficients. As illustrated in Fig. 24c, the drift capacity of the walls decreases approximately linearly with increasing friction coefficient (R-squared value = 0.9689). Furthermore, an increase in the friction coefficient also results in a linear increase in the average equivalent damping ratio before failure of the studied mortarless interlocking brick walls (R-squared value = 0.9834), as shown in Fig. 24d. This is primarily due to the more severe material damage within walls with higher friction coefficients. Fig. 26a and b compare the friction energy dissipation and material damage energy dissipation for walls F1 to F4. It is observed that within the considered range of friction coefficients, the variation in friction energy dissipation is not significant. This is because, even though an increase in the friction coefficient enhances the frictional force between the bricks, the relative sliding displacement decreases as mentioned earlier, thus resulting in insignificant change in friction energy dissipation. However, with higher friction coefficients, the damage condition is more severe at the same drift ratio, causing more energy to be dissipated by material damage, and thus the equivalent damping ratio of the wall increases with the friction coefficient.

7. Analytical predictions

To assist the prediction of the response and capacity of mortarless interlocking brick walls under in-plane cyclic loading, analytical derivations are carried out to estimate their lateral strength, drift capacity and equivalent damping ratio.

7.1. Lateral strength

Generally, the in-plane lateral strength of reinforced masonry walls is composed of three contributions: masonry material strength, the effect of axial stress, and transverse reinforcement [15,16]. For instance, Equation (8) from TMS 402/602-16 [18], which is empirically derived from the research presented in Shing et al. [82] and Shing et al. [28], and Equation (9) from CSA S304-14 (R2019) [17], both adhere to this format. As expressed in Equations (8) and (9), γ_{g1} and γ_{g2} are the reduction factor for partially grouted walls; $\frac{M}{VL}$ equals the ratio of the shear span of the wall to its length, i.e., the shear span ratio; A_n is the net cross-section area; $f_m^{'}$ is the masonry compressive strength; P is the axial load on the wall; f_{yh} is the yield strength of the horizontal reinforcing steel; A_h is the cross-section

Table 13
Design parameters of interlocking brick wall with varying friction coefficients.

No.	Wall length (mm)	Wall height (mm)	Wall thickness (mm)	Shear span (mm)	Axial precompre-ssion (MPa)	Vertical reinforcement	Friction coefficient
F1	2400	2125	100	2500	0.47	4ø20	0.3
F2							0.5
F3							0.7
F4							1.0

Table 14
Simulation results of the interlocking brick walls with varying friction coefficients.

No.	Peak lateral force (kN)	Peak average shear stress (MPa)	Drift capacity	Average equivalent damping ratio around the peak load
F1	111.30	0.464	6.79%	10.99%
F2	115.29	0.480	6.43%	11.89%
F3	115.33	0.480	5.98%	12.53%
F4	114.22	0.476	5.69%	14.36%

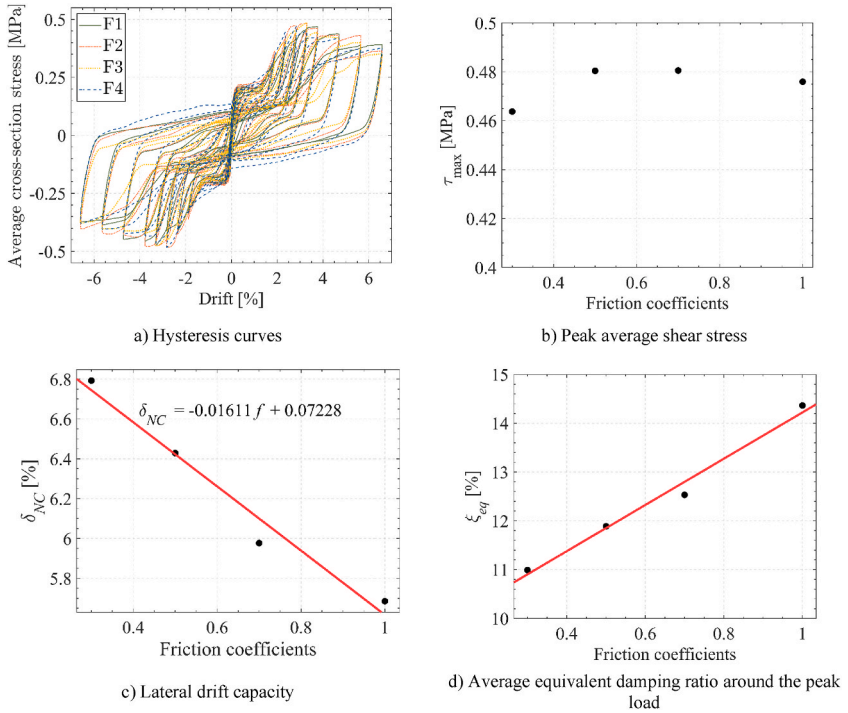

Fig. 24. Simulation results of interlocking brick wall with various friction coefficients. a) Hysteresis curves, b) Peak average shear stress, c) Lateral drift capacity, d) Average equivalent damping ratio around the peak load.

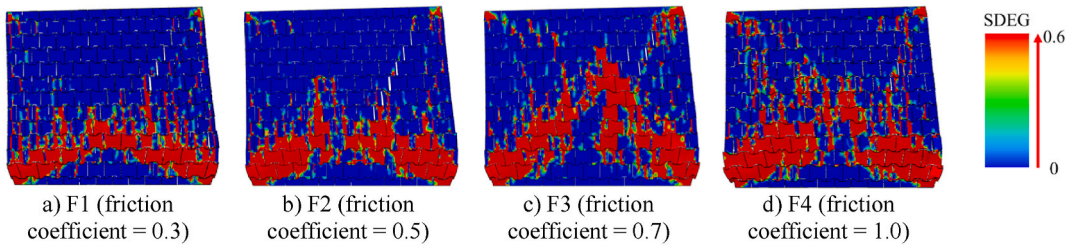

Fig. 25. Damage of the walls with different friction coefficients at 5.7% drift ratio. a) F1 (friction coefficient = 0.3), b) F2 (friction coefficient = 0.5), c) F3 (friction coefficient = 0.7), d) F4 (friction coefficient = 1.0).

area of the horizontal reinforcement; L is the wall length; s_h is the spacing of the horizontal reinforcement; t is the wall thickness. The first term represents the contribution of masonry material strength, including both mortar strength and masonry unit strength; the second term reflects the strength enhancement due to axial precompression; the third term considers the contribution of transverse reinforcement. For the mortarless interlocking brick walls studied in this paper, there is neither mortar nor transverse reinforcement. Instead, according to the simulation results in the above sections, the lateral strength of the wall is contributed by the strength of the brick material and the strength enhancement caused by axial compression, and meanwhile is related to the wall-to-brick size ratio but barely correlated to the friction coefficient between bricks.

As found above in Sections 6.1 and 6.2, both axial precompression and length-to-shear span ratio are linearly correlated with the lateral strength of mortarless interlocking brick walls (Figs. 19b and 21b). Therefore, referring to Equations (8) and (9), the in-plane lateral load-carrying capacity of mortarless interlocking brick walls with shear dominated failure mode can be predicted by Equation

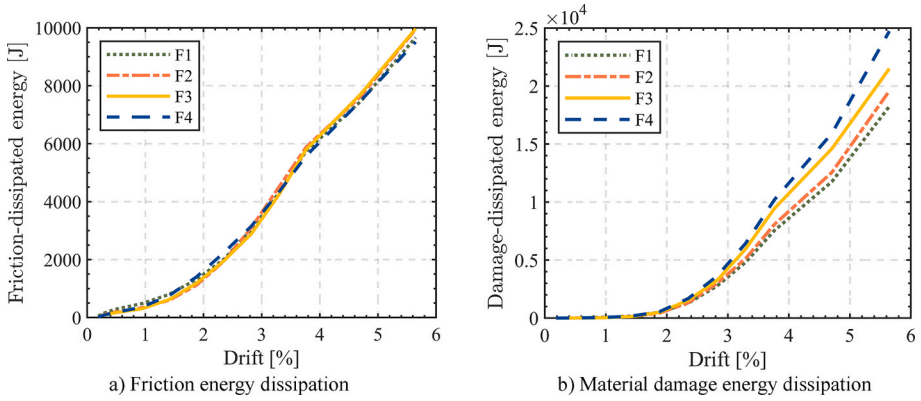

Fig. 26. Energy dissipation by different mechanisms of the walls with varying friction coefficients. a) Friction energy dissipation, b) Material damage energy dissipation.

(11), where $H_0 = M/V$ is the shear span of the wall, L is the length of the wall in the shear direction, $f_{s,key}$ is the shear strength of the small shear keys (Fig. 1b), A_{keys} is the cross-section area of all the small shear keys in the considered section of the wall, P is the axial load applied on the wall, C_i $(i = 1, 2, 3)$ are constants to be determined, and γ_s is the scale factor considering the impact of wall-to-brick size ratio. It is to note that, similar to Equations (8) and (9), Equation (11) is not suitable for predicting the lateral load-carrying capacity of the studied mortarless interlocking brick walls where failure modes are dominated by flexure, either.

In Equation (11), the first term, i.e., $\left[C_1 + C_2\left(\frac{L}{H_0}\right)\right] f_{s,key} A_{keys}$, refers to the lateral strength contributed by brick material strength, corresponding to the first terms of Equations (8) and (9), namely $0.083\left[4.0 - 1.75\left(\frac{M}{VL}\right)\right] A_n \sqrt{f_m'}$ and $0.16\left(2 - \frac{M}{VL}\right)\sqrt{f_m'} Lt$, while the second term, C_3P, corresponds to the term $0.25P$ in Equations (8) and (9), indicating the strength enhancement due to axial pre-compression. It should be noted that, in contrast to Equations (8) and (9), which consider the strength of materials across the entire cross-section of the wall, Equation (11) accounts solely for the cross-sectional area of the small keys (A_{keys}), as depicted in Fig. 1b, on the cross-section of the studied mortarless interlocking brick walls. This is because, according to Ref. [5], when the interlocking brick assembly is subjected to shear load till its failure, the shear strength of the small shear keys (Fig. 1b) controls the overall strength of the interlocking brick assembly. Conservatively, when considering the contribution of brick material strength to the lateral strength of mortarless interlocking brick wall, only the shear strength of the small shear keys, $f_{s,key}$, is included, which can be calculated using Equation (10) [5], where f_b' is the compressive strength of the brick material (differing from the masonry compressive strength f_m') and p is the pre-compressive stress applied on the wall. The cross-section area of the small keys on each interlocking brick, A_{key}, is 7036 mm^2 [5]. A second distinction within Equation (11), as opposed to Equations (8) and (9), lies in the relationship between the wall strength and the shear span-to-length ratio. While the load-carrying capacity is linearly related to the shear span-to-length ratio ($\frac{M}{VL}$) in Equations (8) and (9), Fig. 21b indicates that, for the studied mortarless interlocking brick walls, the lateral strength is linearly related to the length-to-shear span ratio ($\frac{L}{H_0}$). Consequently, in Equation (11), the shear span-to-length ratio ($\frac{M}{VL}$) from Equations (8) and (9) is substituted with the length-to-shear span ratio ($\frac{L}{H_0}$). Additionally, as ungrouted walls are the focus of this study, Equation (11) does not incorporate the reduction coefficient for partially grouted walls as is included in Equations (8) and (9). However, as revealed in Section 5.2, the wall-to-brick size ratio has an impact on the lateral strength of the studied mortarless interlocking brick walls. Therefore, a scale factor related to this ratio, γ_s, has been introduced.

Incorporating the data from walls P1–P5 and L2-L5 and setting $\gamma_s = 1$ for those walls, a multivariate regression analysis is conducted, yielding the values for coefficients C_1 ~C_3 in Equation (11): $C_1 = 0.196$, $C_2 = 0.1504$, and $C_3 = 0.1555$, as shown in Equation (12). The coefficient of determination (R-squared) for this fit is 0.9957, and the root mean square error (RMSE) is 3.00 kN, demonstrating the accuracy of the adopted form in Equation (11) in predicting the lateral strength of the studied interlocking masonry walls.

$$V_{n1} = \gamma_{g1}\left\{0.083\left[4.0 - 1.75\left(\frac{M}{VL}\right)\right] A_n \sqrt{f_m'} + 0.25P + 0.5 f_{yh} A_h \left(\frac{L}{s_h}\right)\right\} \tag{8}$$

$$V_{n2} = \gamma_{g2}\left[0.16\left(2 - \frac{M}{VL}\right)\sqrt{f_m'}\, Lt + 0.25P\right] + 0.6 f_{yh} A_h \left(\frac{L}{s_h}\right) \tag{9}$$

$$f_{s,key} = \left[0.14 + \left(-0.002 f_b' + 0.10076\right)p\right] f_b' \tag{10}$$

$$V_{IB} = \gamma_s\left\{\left[C_1 + C_2\left(\frac{L}{H_0}\right)\right] f_{s,key} A_{keys} + C_3 P\right\} \tag{11}$$

$$V_{IB} = \gamma_s \left\{ \left[0.196 + 0.1504 \left(\frac{L}{H_0} \right) \right] f_{s,key} A_{keys} + 0.1555 P \right\} \tag{12}$$

$$\gamma_s = \begin{cases} -0.01 \dfrac{H}{h_b} + 1.122, \text{when } \dfrac{H}{h_b} \le 10.37 \\ 0.87, \text{when } \dfrac{H}{h_b} > 10.37 \end{cases} \tag{13}$$

It is worth noting that the coefficients related to the shear span ratio and axial load in Equation (12) differ from those obtained in Figs. 19b and 21b. This indicates that there is a certain coupling effect between the influence of axial force and shear span ratio on the lateral strength of mortarless interlocking brick walls [16]. For instance, the first term of Equation (12) is not only related to the shear span ratio of the wall, but also depends on the precompression applied on the wall that affects the shear strength of the interlocking key, $f_{s,key}$, as shown in Equation (10). Such interrelationship explains the difference in coefficients obtained in the multivariate regression analysis compared to those in the univariate regression analyses shown in Figs. 19b and 21b.

Finally, it is essential to determine the scale factor related to the wall-to-brick size ratio. As indicated in Section 5.2, a lower wall-to-brick height ratio results in a higher utilisation efficiency of the brick material, leading to greater peak average shear stress. Conversely, a higher ratio results in reduced material utilisation and a tendency for larger out-of-plane deformations, thereby reducing the in-plane load-bearing capacity. The complex relationship between the wall-to-brick height ratio and the wall's lateral strength involves factors such as the number and transfer efficiency of compressive struts (Section 5.2), the influence of axial compression applied to the wall, and the effect of the wall's height-to-thickness ratio on its out-of-plane stability, which are beyond the scope of this study. Hence, without delving into the principles of the size effect, the scale factor is estimated based on the simulation results of walls S1 to S3. Specifically, the peak average shear stress for wall S1 with a wall-to-brick height ratio of 5.24 is 0.509 MPa, for wall S2 with a ratio of 10.37 is 0.48 MPa, and for wall S3 with a ratio of 15.49 is 0.417 MPa. Taking the ratio of wall S2 (10.37) as a baseline, linear interpolation based on the simulation results of walls S1 and S2 is used for walls with a wall-to-brick height ratio less than or equal to that of S2, to reflect the increase of in-plane lateral strength due to increased material utilisation efficiency as the ratio decreases; for walls with a ratio greater than that of S2, considering the potential for out-of-plane instability, to ensure safety, the factor γ_s has been taken as a reduction coefficient, whose value is determined as the ratio of the peak strength of wall S3, which experiences out-of-plane instability, to that of wall S2, which does not exhibit such instability. The results are illustrated in Equation (13), where h_b represents the height of a single interlocking brick and H stands for the wall height.

Table 15 compares the prediction from Equation (12) and the above simulations, which reveals low discrepancy substantiating the accuracy of Equation (12) for predicting the lateral strength of mortarless interlocking brick walls. It is noted that as wall L1 exhibits flexural failure, a scenario not applicable to Equation (12), and walls L3, S2 and F3 are identical to P3, these walls are excluded.

7.2. Drift capacity

Drift ratio is another parameter commonly considered for masonry structures. For instance, Eurocode 8 - Part 3 [79] recommends 0.4% being the drift limit for significant-damage (SD) limit state, while the near-collapse (NC) limit state drift capacity is considered to be 4/3 times the SD limit drift, i.e., 0.53%. FEMA 273 [94] gives 0.4% as the NC limit state drift capacity of masonry structures. New Zealand standard for seismic assessment [95] also recommends an ultimate limit state (similar to the SD limit state in Eurocode 8-Part 3 [23]) drift capacity of 0.4% for rectangular-section masonry walls and 0.6% for masonry walls with flanges. An exception is the Swiss code SIA D0237 [23,96], in which the drift capacity for masonry walls is considered to be a function of the boundary conditions and precompression of the wall, as shown in Equation (14), where δ_0 is the benchmark drift capacity, p is the precompression applied on the wall, and $f_m^{'}$ is the masonry compressive strength. When the wall is a cantilever wall, $\delta_0 = 0.8\%$; when the wall is fixed at both ends, δ_0

Table 15
Comparison of lateral strength between simulation results and the results from Equation (12).

Case name	Wall length (mm)	Wall height (mm)	Shear span (mm)	Wall length-to-shear span ratio	Wall-to-brick height ratio	Friction coefficient between bricks	Axial compression (MPa)	Simulated peak average shear stress (MPa)	Peak average shear stress predicted by Equation (12) (MPa)	Relative error of Equation (12)
P1	2400	2125	2500	0.96	10.37	0.7	0.235	0.404	0.403	−0.04%
P2							0.3525	0.439	0.438	−0.23%
P3							0.47	0.480	0.472	−1.64%
P4							0.5875	0.518	0.506	−2.26%
P5							0.705	0.535	0.540	1.02%
L2	1800			0.72			0.47	0.402	0.429	6.79%
L4	3000			1.2				0.521	0.515	−1.15%
L5	3600			1.44				0.552	0.557	1.06%
S1	1200	1075	1250	0.96	5.24			0.509	0.500	−0.85%
S3	3600	3175	3750		15.49			0.417	0.410	−1.61%
F1	2400	2125	2500		10.37	0.3		0.464	0.472	1.76%
F2						0.5		0.480		−1.64%
F4						1.0		0.476		−0.81%

= 0.4%. To further account for the size effect, i.e., the size ratio between the wall and the brick [24], Petry and Beyer [23] modified Equation (14), resulting in Equation (15) as presented. Herein, H_0 represents the shear span, H is the wall height, and H_{ref} is the reference wall height, taken as H_{ref} = 2400 mm.

For mortarless interlocking brick walls, the drift capacity is significantly influenced by the precompression level (Fig. 19c) and is also related to the friction coefficient between bricks (Fig. 24c) as well as the wall-to-brick size ratio (Table 8), but essentially unrelated to the shear span ratio when the wall exhibits shear failure (Fig. 21c). Consequently, as opposed to the approach of considering the drift capacity of masonry walls as a fixed value in standards such as Eurocode 8 - Part 3 [79] and FEMA 273 [94], the calculation method for drift capacity provided in SIA D0237 [96] and by Petry and Beyer [23] is more suitable for the drift capacity of the studied mortarless interlocking brick walls. Thus, referencing Equation (15), the drift capacity of the studied mortarless interlocking brick walls failing in shear is expressed in the form of Equation (16), where μ represents the friction coefficient between the interlocking bricks, and δ_0, C_1, C_2, β are constants, with β being correspondent to the size effect-related factor $\left(\frac{H_{ref}}{H}\right)^{0.5}$ in Equation (15). In this study, $f_m^{'}$ = 8.1 MPa as described in Section 6.1, and H_{ref} is taken as 2125 mm in accordance with the height of the benchmark model validated in Section 4. Compared to Equation (15), Equation (16) incorporates a linear factor $(1 - C_2\mu)$ related to the friction coefficient, reflecting the linear relationship between the friction coefficient between bricks and the wall's drift capacity as shown in Fig. 24c. Additionally, as indicated in Section 5.2, in the studied mortarless interlocking brick walls, a larger $\frac{H_{ref}}{H}$, i.e., a smaller wall-to-brick height ratio, leads to more significant material failure and hence, a reduced drift capacity; a smaller $\frac{H_{ref}}{H}$, i.e., a larger wall-to-brick height ratio, implies more pronounced out-of-plane deformation affecting the wall's in-plane performance, also resulting in a reduced drift capacity. Therefore, in a similar way as used to determine the size-related factor in Section 7.1, β are calculated separately for conditions where the wall-to-brick height ratio is smaller than or equal to that of S2 and where the ratio is greater than that of S2, based on the numerical simulation results of walls S1–S3. When the wall-to-brick height ratio does not exceed that of S2, β takes the form of $\left(\frac{H_{ref}}{H}\right)^{\kappa}$ as in Equation (15), where κ is a non-dimensional coefficient to be determined by fitting; when the wall-to-brick height ratio is larger than that of S2, for safety reasons, β is taken as a reduction factor, whose value is the ratio of the drift capacity of wall S3, where out-of-plane instability occurs, to that of wall S2, where no such instability emerges. The outcomes are depicted in Equation (17). Ultimately, through regression analysis based on the above simulation results, Equation (16) yields δ_0 = 10.41%, C_1 = 7.204, and C_2 = 0.2805, as shown in Equation (18). The coefficient of determination (R-squared) for this fit is 0.8963, and the root mean square error (RMSE) is 0.5207%.

$$\delta_{NC} = \frac{4}{3}\delta_0\left(1 - 2.4\frac{p}{f_m^{'}}\right) \tag{14}$$

$$\delta_{NC} = 1.3\%\left(1 - 2.2\frac{p}{f_m^{'}}\right)\ \frac{H_0}{H}\left(\frac{H_{ref}}{H}\right)^{0.5} \tag{15}$$

$$\delta_{NC} = \delta_0\left(1 - C_1\frac{p}{f_m^{'}}\right)\ \frac{H_0}{H}\beta(1 - C_2\mu) \tag{16}$$

$$\beta = \begin{cases} \left(\frac{H_{ref}}{H}\right)^{-0.239}, \text{when } \frac{H}{h_b} \le 10.37 \\ 0.846, \text{when } \frac{H}{h_b} > 10.37 \end{cases} \tag{17}$$

Table 16
Comparison of drift capacity between simulation results and the results from Equation (18).

Case name	Wall length (mm)	Wall height (mm)	Shear span (mm)	Wall length-to-shear span ratio	Wall-to-brick height ratio	Friction coefficient between bricks	Axial compression (MPa)	Simulated drift capacity	Drift capacity predicted by Equation (18)	Relative error of Equation (18)
P1	2400	2125	2500	0.96	10.37	0.7	0.235	7.49%	7.78%	3.87%
P2							0.3525	6.46%	6.75%	4.49%
P3							0.47	5.98%	5.72%	−4.35%
P4							0.5875	3.90%	4.69%	20.26%
P5							0.705	3.62%	3.66%	1.10%
L2	1800			0.72			0.47	5.44%	5.72%	5.15%
L4	3000			1.2				5.25%		8.95%
L5	3600			1.44				5.61%		1.96%
S1	1200	1075	1250	0.96	5.24			5.08%	4.80%	−5.51%
S3	3600	3175	3750		15.49			5.06%	4.86%	−3.95%
F1	2400	2125	2500		10.37	0.3		6.79%	6.52%	−3.98%
F2						0.5		6.43%	6.12%	−4.82%
F4						1.0		5.69%	5.12%	−10.02%

$$\delta_{NC} = 10.41\%\left(1 - 7.204\frac{p}{f_m'}\right)\frac{H_0}{H}\beta(1 - 0.2805\mu) \tag{18}$$

Table 16 compares the predictions from Equation (18) and the simulation results, where small errors are revealed. For the same reasons as stated in Section 7.1, cases L1, L3, S2 and F3 are not included in Table 16.

7.3. Equivalent damping ratio

To estimate the equivalent damping ratio, some equations have been proposed for masonry walls with a rocking failure mode [83, 97–99], while it is more common to specify a damping ratio or a range of damping ratios for walls with a diagonal shear cracking failure mode [83,86,100–102]. Unlike previous studies, the equivalent damping ratios for mortarless interlocking brick walls (between reaching 80% of the peak load for the first time and dropping to 80% of peak strength during the degradation stage) shows an approximately linear relationship with the axial precompression, the wall's length-to-shear span ratio, and the friction coefficient between the bricks. It thus enables the derivation of an equation to estimate the equivalent damping ratio. A reasonable equation that considers the aforementioned linear relationships is presented as Equation (19), where α, ξ_{eq0}, C_1, C_2 and C_3 are all constants, of which α is the scale factor related to the size effect observed in Section 5.2, calculated based on the simulation results of walls S1, S2 and S3. As shown in Table 8, walls with a lower wall-to-brick size ratio (as exemplified by wall S1) exhibit a higher average equivalent damping ratio around the peak strength. In contrast, a larger wall-to-brick size ratio (as with wall S3) may lead to significant out-of-plane deformations, initiating strength degradation at smaller drift ratios, and thus reducing the average equivalent damping ratio around the peak strength of the wall. Assuming a linear relationship between the wall-to-brick size ratio and the equivalent damping ratio for wall-to-brick size ratios less than or equal to that of wall S2, and a fixed value of α for wall-to-brick size ratios greater than that of wall S2 for safety reasons (taken as the ratio of the equivalent damping ratio of wall S3 to that of wall S2, as in Sections 7.1 and 7.2), α is calculated according to Equation (20).

Based on the multivariate regression analysis using above simulation results, the values of other constants are obtained as $\xi_{eq0} = 3.51\%$, $C_1 = 0.486$, $C_2 = 1.2062$, and $C_3 = 0.7435$, as shown in Equation (21). The coefficient of determination (R^2) for the fitting is 0.925, and the root mean square error (RMSE) is 0.47%. The relatively high R-squared (over 0.9) value and the low RMSE compared to the mean value of the equivalent damping ratios in the simulated cases (12.84%) demonstrate the accuracy of the fitting.

Table 17 compares the predictions using Equation (21) and the corresponding results from numerical simulations, which reveals less than 10% error. To note, for the same reasons as stated in Sections 7.1 and 7.2, cases L1, L3, S2 and F3 are not included.

$$\xi_{eq} = \alpha\xi_{eq0}\left(1 + C_1\frac{p}{f_m'}\right)\left(1 + C_2\frac{L}{H_0}\right)(1 + C_3\mu) \tag{19}$$

$$\alpha = \begin{cases} -2.41 \times 10^{-2}\dfrac{H}{h_b} + 1.25, \text{when } \dfrac{H}{h_b} \le 10.37 \\ 0.98, \text{when } \dfrac{H}{h_b} > 10.37 \end{cases} \tag{20}$$

$$\xi_{eq} = 3.51\%\alpha\left(1 + 0.486\frac{p}{f_m'}\right)\left(1 + 1.2062\frac{L}{H_0}\right)(1 + 0.7435\mu) \tag{21}$$

Table 17
Comparison of equivalent damping ratio between simulation results and the results from Equation (21).

Case name	Wall length (mm)	Wall height (mm)	Shear span (mm)	Wall length-to-shear span ratio	Wall-to-brick height ratio	Friction coe-fficient between bricks	Axial compression (MPa)	Simulated average equivalent damping ratio around the peak load	Average equivalent damping ratio around the peak load predicted by Eqn 21	Relative error of Eqn 21
P1	2400	2125	2500	0.96	10.37	0.7	0.235	9.41%	10.35%	9.99%
P2							0.3525	11.91%	11.50%	−3.44%
P3							0.47	12.53%	12.64%	0.88%
P4							0.5875	13.65%	13.78%	0.95%
P5							0.705	14.27%	14.93%	4.63%
L2	1800			0.72			0.47	11.99%	11.32%	−5.59%
L4	3000			1.2				13.75%	13.96%	1.53%
L5	3600			1.44				15.73%	15.27%	−2.92%
S1	1200	1075	1250	0.96	5.24			14.08%	14.20%	0.85%
S3	3600	3175	3750		15.49			12.36%	12.39%	0.24%
F1	2400	2125	2500		10.37	0.3		10.99%	10.81%	−1.64%
F2						0.5		11.89%	11.72%	−1.43%
F4						1.0		14.36%	14.01%	−2.44%

8. Conclusions

This paper employs numerical simulations to perform a comprehensive study on the in-plane cyclic behaviour of mortarless interlocking brick walls with aim to provide guidance for the engineering practice. Parametric studies are conducted based on a detailed numerical model, which is validated using data from laboratory cyclic tests and is subsequently employed to investigate the influences of various factors on the behaviour of interlocking brick walls under cyclic loading. These factors include reinforcement grouting methods, wall-to-brick size ratio, axial precompression, wall shear span ratio, and the friction coefficient between bricks. Analytical models are summarised to facilitate the strength-based design of the studied mortarless interlocking brick wall. The following conclusions are drawn:

1. For the studied mortarless interlocking brick walls, grouting vertical reinforcements improves wall lateral strength. However, walls with unbonded reinforcements outperform in terms of deformability and residual deformation. As a result, this study primarily investigates the performance of mortarless interlocking brick walls with unbonded reinforcements.
2. The wall-to-brick size ratio significantly impacts the performance of mortarless interlocking brick walls. A lower ratio results in a higher material utilisation and consequently a higher lateral strength. However, it also leads to earlier material damage, reducing the ductility of the wall. Conversely, a higher ratio may lead to pronounced out-of-plane deformations, affecting both lateral strength and ductility.
3. The in-plane lateral strength of the studied mortarless interlocking brick walls failing in diagonal shear increases linearly with the applied axial precompression and the length-to-shear span ratio. It is also related to the relative size of the wall to the brick. An equation considering the wall's axial force, shear span ratio, and the relative size of the wall to the brick has been proposed to estimate the in-plane lateral strength of walls with a diagonal shear failure mode. Its accuracy has been affirmed by numerical simulation results.
4. The in-plane drift capacity of the studied mortarless interlocking brick walls failing in diagonal shear cracking mode linearly decreases with increasing applied precompression and increasing friction coefficient between the bricks. An equation incorporating the wall's axial compression and the friction coefficient between bricks, while considering the relative size of the wall to the bricks, has been introduced to estimate the in-plane drift capacity of the walls. Its precision has been confirmed by comparison with numerical simulation results.
5. The equivalent damping ratio of the mortarless interlocking brick walls exhibits a linear increase with applied axial precompression, length-to-shear span ratio, and friction coefficient between bricks. An equation has been formulated to estimate the equivalent damping ratio of the walls based on these observations, with its accuracy validated against numerical simulation results.

It is imperative to note that this study is based on numerical simulations, which allow for the exploration of mortarless interlocking brick wall performance under in-plane quasi-static cyclic loading with various design parameters at a lower economic cost and in a shorter timeframe than lab tests or engineering practice. However, the idealised boundary conditions used in the numerical simulations differ from those encountered in actual engineering projects or lab tests, introducing potential limitations. Additionally, imperfections in geometric dimensions and material properties in real engineering situations could impact the in-plane performance of the studied mortarless interlocking brick walls. Further research, encompassing both numerical simulations and actual experimental tests, is required to validate the conclusions derived in this manuscript. Moreover, the material properties of the bricks in this numerical study have been defined based on those of rammed earth measured in previous material tests. In engineering practice, bricks can be made of materials such as clay, ceramics, etc., in addition to rammed earth. The validity and precision of the findings when using these other materials remain to be examined. Furthermore, as discerned from Section 5.2, the relative size of the wall to the brick exerts a significant influence on the performance of the studied mortarless interlocking brick walls. Varying wall-to-brick size ratios affect material utilisation efficiency and may increase the likelihood of out-of-plane instability. Detailed quantitative studies on the size effect for mortarless interlocking brick walls, as well as how it is coupled with factors such as applied precompression and the friction coefficient between bricks, warrant further investigation. Finally, it should be noted that the analytical equations proposed in this study are applicable to mortarless interlocking brick walls with a diagonal shear failure mode. The investigation into the lateral strength, deformability, and energy dissipation characteristics of walls that fail in flexure remains an area for future research.

CRediT authorship contribution statement

Guanyu Xie: Data curation, Formal analysis, Investigation, Software, Visualization, Writing – original draft. **Xihong Zhang:** Funding acquisition, Methodology, Project administration, Resources, Supervision, Validation, Writing – review & editing. **Hong Hao:** Conceptualization, Project administration, Resources, Supervision, Writing – review & editing. **Joyis Thomas:** Resources.

Declaration of competing interest

The authors declare that they have no known competing financial interests or personal relationships that could have appeared to influence the work reported in this paper.

Data availability

Data will be made available on request.

Acknowledgements

The authors would like to acknowledge the financial support from Australian Research Council (ARC) for conducting this study.

References

[1] K. Ramamurthy, E.K. Kunhanandan Nambiar, Accelerated masonry construction review and future prospects, Prog. Struct. Eng. Mater. 6 (2004) 1–9.
[2] G. Peirs, Masonry in the third millennium, in: H.W.H. West, S. British Masonry (Eds.), Masonry (8), British Masonry Society, 1998, pp. 6–8.
[3] J.A. Thamboo, T. Zahra, R. Dhanasekar, Development of design methodology for mortarless masonry system: case study – a resettlement housing colony, J. Build. Eng. 27 (2020).
[4] T. Shi, X. Zhang, H. Hao, C. Chen, Experimental and numerical investigation on the compressive properties of interlocking blocks, Eng. Struct. 228 (2021) 111561.
[5] T. Shi, X. Zhang, H. Hao, G. Xie, Experimental and numerical studies of the shear resistance capacities of interlocking blocks, J. Build. Eng. 44 (2021) 103230.
[6] T. Sturm, L.F. Ramos, P.B. Lourenço, Characterization of dry-stack interlocking compressed earth blocks, Mater. Struct. 48 (2015) 3059–3074.
[7] H. Liu, P. Liu, K. Lin, S. Zhao, Cyclic behavior of mortarless brick joints with different interlocking shapes, Materials 9 (2016) (Basel, Switzerland).
[8] K. Lin, H.J. Liu, Y.Z. Totoev, Quasi-static experimental research on dry-stack masonry infill panel frame (in Chinese), J. Build. Struct. 33 (2012) 119–127.
[9] A. Elvin, H.C. Uzoegbo, Response of a full-scale dry-stack masonry structure subject to experimentally applied earthquake loading, J. S. Afr. Inst. Civ. Eng. 53 (2011) 22–32.
[10] M. Dhanasekar, W. Haider, Effect of spacing of reinforcement on the behaviour of partially grouted masonry shear walls, Adv. Struct. Eng. 14 (2011) 281–293.
[11] K. Lin, Y.Z. Totoev, H. Liu, A.W. Page, Modeling of dry-stacked masonry panel confined by reinforced concrete frame, Arch. Civ. Mech. Eng. 14 (2014) 497–509.
[12] M. Kohail, Behavior of Masonry Walls Constructed Using Locally Available Dry-Stack Interlocking Masonry Units [PhD], Ain Shams University, 2015.
[13] G. Xie, X. Zhang, H. Hao, K. Bi, Y. Lin, Response of reinforced mortar-less interlocking brick wall under seismic loading, Bull. Earthq. Eng. 20 (2022) 6129–6165.
[14] G. Xie, X. Zhang, H. Hao, J. Thomas, Response of mortar-free interlocking brick wall under seismic excitation, in: Proceedings of 2020 Australian Earthquake Engineering Society Conference, Australian Earthquake Engineering Society, Virtual, 2020, pp. 309–316.
[15] M. Bolhassani, A.A. Hamid, C. Johnson, A.E. Schultz, Shear strength expression for partially grouted masonry walls, Eng. Struct. 127 (2016) 475–494.
[16] R. Hassanli, M.A. ElGawady, J.E. Mills, An evaluation of design code expressions for estimating in-plane shear strength of partiallY grouted masonry walls, Aust. J. Struct. Eng. 15 (2014) 299–320.
[17] C.S. Association, in: CSA S304-14 (R2019): Design of Masonry Structures, third ed. ed, CSA Group, Mississauga, Ontario, 2014.
[18] Building Code Requirements and Specification for Masonry Structures: TMS 402/602-16, The masonry society, Longomont, 2016.
[19] S.N. Zealand, Design of Reinforced Concrete Masonry Structures: NZS 4230:2004, Standards New Zealand, Wellington, New Zealand, 2004.
[20] China MoHaU-RDotPsRo, GB 50003-2011: code for design of masonry structures (in Chinese), in: National Standard of the People's Republic of China, China Architecture & Building Press, Beijing, 2011.
[21] T. Celano, L.U. Argiento, F. Ceroni, C. Casapulla, Literature review of the in-plane behavior of masonry walls: theoretical vs. Experimental results, Materials 14 (2021) (Basel, Switzerland).
[22] S. Szabó, M.F. Funari, P.B. Lourenço, Masonry patterns' influence on the damage assessment of URM walls: current and future trends, Dev. Built Environ. 13 (2023).
[23] S. Petry, K. Beyer, Influence of boundary conditions and size effect on the drift capacity of URM walls, Eng. Struct. 65 (2014) 76–88.
[24] K.M. Dolatshahi, M.T. Nikoukalam, K. Beyer, Numerical study on factors that influence the in-plane drift capacity of unreinforced masonry walls, Earthq. Eng. Struct. Dynam. 47 (2018) 1440–1459.
[25] K.C. Voon, J.M. Ingham, Experimental in-plane shear strength investigation of reinforced concrete masonry walls, J. Struct. Eng. 132 (2006) 400–408.
[26] F. Ahmadi Koutalan, Displacement-based Seismic Design and Tools for Reinforced Masonry Shear-Wall Structures, University of Texas at Austin, Austin, Texas, 2012.
[27] T. Kasparik, M.J. Tait, W.W. El-Dakhakhni, Seismic performance assessment of partially grouted, nominally reinforced concrete-masonry structural walls using shake table testing, J. Perform. Constr. Facil. 28 (2014) 216–227.
[28] P.B. Shing, M. Schuller, V.S. Hoskere, E. Carter, Flexural and shear response of reinforced masonry walls, ACI Struct. J. 87 (1990) 646–656.
[29] P. Morandi, G. Magenes, Experimental and numerical researches in support of seismic design of masonry buildings. Future Trends in Civil Engineering, Faculty of Civil Engineering, University of Zagreb, Zagreb, Croatia, 2014.
[30] S. Dorji, H. Derakhshan, D.P. Thambiratnam, T. Zahra, A. Mohyeddin, Behaviour and material properties of versaloc semi-interlocking mortarless masonry, Mater. Struct. 56 (2023).
[31] T. Zahra, J. Dorji, J. Thamboo, N. Cameron, M. Asad, W. Kasinski, et al., Behaviour of reinforced mortarless concrete masonry panels under axial compression: an experimental and analytical study, Construct. Build. Mater. 377 (2023).
[32] T. Zahra, J. Dorji, J. Thamboo, M. Asad, W. Kasinski, A. Nardone, In-plane and out-of-plane shear characteristics of reinforced mortarless concrete block masonry, J. Build. Eng. 66 (2023).
[33] T. Zahra, M. Dhanasekar, Characterisation and strategies for mitigation of the contact surface unevenness in dry-stack masonry, Construct. Build. Mater. 169 (2018) 612–628.
[34] B. Qu, B.J. Stirling, D.C. Jansen, D.W. Bland, P.T. Laursen, Testing of flexure-dominated interlocking compressed earth block walls, Construct. Build. Mater. 83 (2015) 34–43.
[35] D.W. Bland, In-Plane Cyclic Shear Performance of Interlocking Compressed Earth Block Walls, San Luis Obispo, California: California Polytechnic State University, 2011.
[36] M. Kohail, H. Elshafie, A. Rashad, H. Okail, Behavior of post-tensioned dry-stack interlocking masonry shear walls under cyclic in-plane loading, Construct. Build. Mater. 196 (2019) 539–554.
[37] A. Gul, B. Alam, K. Shahzada, Seismic performance evaluation of unconfined dry stacked block masonry structure, Eng. Struct. 265 (2022).
[38] A. Gul, B. Alam, I.U. Khan, S.A.A. Shah, S.W. Khan, K. Shahzada, Improving seismic capacity of dry stacked interlocking masonry structure through confinement at corners, Soil Dynam. Earthq. Eng. 165 (2023).
[39] G. Xie, X. Zhang, H. Hao, T. Shi, L. Cui, J. Thomas, Behaviour of reinforced mortarless interlocking brick wall under cyclic loading, Eng. Struct. 283 (2023).
[40] M. Ali, R. Briet, N. Chouw, Dynamic response of mortar-free interlocking structures, Construct. Build. Mater. 42 (2013) 168–189.
[41] M. Ishfaq, A. Ullah, A. Ahmed, S. Ali, S.M. Ali, M. Uddin, et al., Numerical approximation of blast loads on confined dry-stacked masonry wall, Math. Probl Eng. 2021 (2021) 1–13.
[42] I. Ali, A. Noreen, Z. Akbar, A. Khan, A. Ullah, A review on numerical modelling of dry-stacked masonry wall against blast load. 1st International Conference on Advances in Civil & Environmental Engineering, University of Engineering & Technology, Taxila, Pakistan, 2022.
[43] A. Ullah, K. Shahzada, S. Ali, S. Mohammad Ali, A. Gul, Performance evaluation of confined dry-stacked block masonry against blast loading, Structures 45 (2022) 58–71.
[44] A.V. Dyskin, E. Pasternak, J.S. Estrin, D.H.T. Yong, H.C. Khor, Construction block, in: E.P. Office (Ed.), E01C5/00, Europe: Tetraloc Pty Ltd, 2018.
[45] J. Thomas, Technical Details, Tetraloc Pty Ltd., Bellevue WA, 2019.
[46] A.V. Dyskin, Y. Estrin, E. Pasternak, H.C. Khor, A.J. Kanel-Belov, Fracture resistant structures based on topological interlocking with non-planar contacts, Adv. Eng. Mater. 5 (2003) 116–119.

[47] M. Dhanasekar, W. Haider, T. Janaraj, Response of partially grouted wider reinforced masonry walls to inplane cyclic shear, in: S. Serega, A. Winnicki (Eds.), Proceedings of the 7th International Conference on Analytical Models and New Concepts in Concrete and Masonry Structures. CD Rom, Cracow University of Technology, 2011, pp. 1–12.
[48] T. Janaraj, M. Dhanasekar, W. Haider, Wider reinforced masonry shear walls subjected to cyclic lateral loading, Archit. Civil Eng. Environ. (ACEE) 4 (2011) 39–46.
[49] W. Haider, Inplane Response of Wide Spaced Reinforced Masonry Shear Walls, Central Queensland University Australia, 2007.
[50] D. Hibbitt, B. Karlsson, P. Sorensen, Abaqus FEA. 2019 FD01, Dassault Systèmes, 2019.
[51] M.K. Howlader, M.J. Masia, M.C. Griffith, In-plane response of perforated unreinforced masonry walls under cyclic loading: experimental study, J. Struct. Eng. 146 (2020) 04020106.
[52] C. Sandoval, S. Calderón, J.L. Almazán, Experimental cyclic response assessment of partially grouted reinforced clay brick masonry walls, Bull. Earthq. Eng. 16 (2018) 3127–3152.
[53] China MoHaU-RDotPsRo, Research CIoBSD, Commonly Used Data in Structure Design: Reinforced Concrete Structure, Masonry Structure, Foundation (in Chinese), China Planning Press, Beijing, 2013.
[54] J. Zhu, N. Shrive, Partially grouted concrete masonry shear walls subject to in-plane shear load: a critical review, Rev. IBRACON de Estrut. e Mater. 16 (2023).
[55] Security USDoH, Agency FEM. Interim Testing Protocols for Determining the Seismic Performance Characteristics of Structural and Nonstructural Components: FEMA 461. Scotts Valley: CreateSpace Independent Publishing Platform.
[56] M. Tomaževič, Earthquake-resistant Design of Masonry Buildings, Imperial College Press, London, 2006.
[57] D. Systèmes, Abaqus Documentation R2022x, 2022.
[58] G. Fortunato, M.F. Funari, P. Lonetti, Survey and seismic vulnerability assessment of the baptistery of san Giovanni in Tumba (Italy), J. Cult. Herit. 26 (2017) 64–78.
[59] Z. Zhuang, Finite Element Analysis and its Application Based on ABAQUS (in Chinese), 1 ed., Tsinghua University Press, Beijing, 2009.
[60] M. Martínez, S. Atamturktur, B. Ross, J. Thompson, Assessing the compressive behavior of dry-stacked concrete masonry with experimentally informed numerical models, J. Struct. Eng. 144 (2018) 04018080.
[61] J. Lubliner, J. Oliver, S. Oller, E. Oñate, A plastic-damage model for concrete, Int. J. Solid Struct. 25 (1989) 299–326.
[62] J. Lee, G.L. Fenves, Plastic-damage model for cyclic loading of concrete structures, J. Eng. Mech. 124 (1998) 892–900.
[63] W. Li, J. Wu, A note on the ABAQUS concrete damaged plasticity (CDP) model. Proceedings of the International Conference on Civil, Architecture and Environmental Engineering (ICCAE2016), CRC Press/Balkema, Taipei, Taiwan, 2017, pp. 1247–1252.
[64] Y. Nie, A. Sheikh, M. Griffith, P. Visintin, J. Vaculik, The Application of Mixed-Mode De-cohesion Criteria in Masonry Finite Element Analysis, Australian Earthquake Engineering Society, Newcastle, New South Wales, 2019. Australian Earthquake Engineering Society 2019 Conference.
[65] A. Al-Ahdal, N. Aly, K. Galal, Simplified analytical models for partially grouted reinforced masonry shear walls, Eng. Struct. 252 (2022) 113643.
[66] Q.-B. Bui, T.-T. Bui, M.-P. Tran, T.-L. Bui, H.-A. Le, Assessing the seismic behavior of rammed earth walls with an L-form cross-section, Sustainability 11 (2019).
[67] Y. Sümer, M. Aktaş, Defining parameters for concrete damage plasticity model, Chall. J. Struct. Mech. 1 (2015) 149–155.
[68] Housing Mo, China U-RDotPso, GB 50010-2010: Code for Design of Concrete Structures, 2015 Edition, China Architecture Publishing & Media Co., Ltd., Beijing, 2016.
[69] Z. Wang, Z. Yu, Concrete damage model based on energy loss (in Chinese), J. Build. Mater. 7 (2004) 365–369.
[70] H. Qin, X. Zhao, Numerical analysis of composite columns with high steel ratio under cyclic loading (in Chinese), Struct. Eng. 30 (2014) 25–31.
[71] S.J. Menegon, H.H. Tsang, J.L. Wilson, N.T.K. Lam, Overstrength and ductility of limited ductile RC walls: from the design engineers perspective. The Tenth Pacific Conference on Earthquake Engineering, Australian Earthquake Engineering Society, Sydney, Australia, 2015.
[72] S. Zhang, D. Yang, Y. Sheng, S.W. Garrity, L. Xu, Numerical modelling of FRP-reinforced masonry walls under in-plane seismic loading, Construct. Build. Mater. 134 (2017) 649–663.
[73] C. Casapulla, F. Portioli, Experimental and analytical investigation on the frictional contact behavior of 3D masonry block assemblages, Construct. Build. Mater. 78 (2015) 126–143.
[74] B.G. Rabbat, H.G. Russell, Friction coefficient of steel on concrete or grout, J. Struct. Eng. 111 (1985) 505–515.
[75] C. Li, H. Hao, K. Bi, Numerical study on the seismic performance of precast segmental concrete columns under cyclic loading, Eng. Struct. 148 (2017) 373–386.
[76] K.F. Abdulla, L.S. Cunningham, M. Gillie, Simulating masonry wall behaviour using a simplified micro-model approach, Eng. Struct. 151 (2017) 349–365.
[77] A. Matsumura, Shear strength of reinforced masonry walls. The Ninth World Conference on Earthquake Engineering, 9WCEE Organizing Committee, Tokyo-Kyoto, Japan, 1988, pp. 121–126.
[78] S. Calderon, L. Vargas, C. Sandoval, G. Araya-Letelier, Behavior of partially grouted concrete masonry walls under quasi-static cyclic lateral loading, Materials 13 (2020) (Basel).
[79] Eurocode 8, Design of Structures for Earthquake Resistance. Part 3, Assessment and Retrofitting of Buildings, British Standards Institution, London, 2006.
[80] P.B. Lourenco, Two aspects related to the analysis of masonry structures: size effect and parameter sensibility. Numerical Models for Masonry Structures and Stacked Construction, Delft University of Technology, Delft, Netherlands, 1997.
[81] S. Petry, K. Beyer, Scaling unreinforced masonry for reduced-scale seismic testing, Bull. Earthq. Eng. 12 (2014) 2557–2581.
[82] P.B. Shing, M. Schuller, V.S. Hoskere, In-plane resistance of reinforced masonry shear walls, J. Struct. Eng. 116 (1990) 619–640.
[83] G. Magenes, G.M. Calvi, In-plane seismic response of brick masonry walls, Earthq. Eng. Struct. Dynam. 26 (1997) 1091–1112.
[84] AS 3700-2018: Masonry Structures, Standards Australia, Sydney, N.S.W., 2018.
[85] Design of Masonry Structures: CSA S304.1-14, third ed. ed, CSA Group, Mississauga, Ontario, 2014.
[86] S. Calderón, C. Sandoval, G. Araya-Letelier, E. Inzunza, O. Arnau, Influence of different design parameters on the seismic performance of partially grouted masonry shear walls, Eng. Struct. 239 (2021) 112058.
[87] S. Calderón, C. Sandoval, E. Inzunza, C. Cruz-Noguez, A.B. Rahim, L. Vargas, Influence of a window-type opening on the shear response of partially-grouted masonry shear walls, Eng. Struct. 201 (2019) 109783.
[88] Z. Zhang, J. Murcia-Delso, C. Sandoval, G. Araya-Letelier, F. Wang, In-plane shear strength and damage fragility functions for partially-grouted reinforced masonry walls with bond-beam reinforcement, Eng. Struct. 242 (2021) 112569.
[89] S. Burnett, M. Gilbert, T. Molyneaux, G. Beattie, B. Hobbs, The performance of unreinforced masonry walls subjected to low-velocity impacts: finite element analysis, Int. J. Impact Eng. 34 (2007) 1433–1450.
[90] K.M. Kareem, E. Ahani, B. Panto, Evaluating simplified macromodeling approaches of simulating infilled reinforced concrete frames with openings, Struct. Concr. 24 (2022) 721–737.
[91] J. Kong, C. Zhai, S. Li, L. Xie, Study on in-plane seismic performance of solid masonry-infilled RC frames, China Civ. Eng. J. 45 (2012) 137–141.
[92] M.A. Hossain, Modelling of Semi Interlocking Masonry Based on Observed Behaviour [PhD Thesis], The University of Newcastle, Newcastle, Australia, 2019.
[93] P.B. Lourenço, J.O. Barros, J.T. Oliveira, Shear testing of stack bonded masonry, Construct. Build. Mater. 18 (2004) 125–132.
[94] F.E.M. Agency, FEMA 273: NEHRP Guidelines for the Seismic Rehabilitation of Buildings, Federal Emergency Management Agency, Washington D.C., 1997.
[95] NZSfE. Engineering, Assessment and Improvement of the Structural Performance of Buildings in Earthquakes, New Zealand Society for Earthquake Engineering, Wellington, N.Z., 2006.
[96] SIA D0237, Evaluation de la sécurité parasismique des bâtiments en maçonnerie (in French), SIA Schweizerischer Ingenieur- und Architektenverein, Zürich, 2011.
[97] U. Tomassetti, F. Graziotti, L. Sorrentino, A. Penna, Modelling rocking response via equivalent viscous damping, Earthq. Eng. Struct. Dynam. 48 (2019) 1277–1296.
[98] M.J.N. Priestley, R.J. Evison, A.J. Carr, Seismic response of structures free to rock on their foundations, Bull. N. Z. Natl. Soc. Earthq. Eng. 11 (1978) 141–150.

[99] G.W. Housner, The behavior of inverted pendulum structures during earthquakes, Bull. Seismol. Soc. Am. 53 (1963) 403–417.
[100] Eurocode 8, Design of Structures for Earthquake Resistance: Part 1: General Rules, Seismic Actions and Rules for Buildings, British Standards Institution, London, 1998.
[101] P. Ramírez, C. Sandoval, J.L. Almazán, Experimental study on in-plane cyclic response of partially grouted reinforced concrete masonry shear walls, Eng. Struct. 126 (2016) 598–617.
[102] H. Ozkaynak, E. Yuksel, C. Yalcin, A.A. Dindar, O. Buyukozturk, Masonry infill walls in reinforced concrete frames as a source of structural damping, Earthq. Eng. Struct. Dynam. 43 (2014) 949–968.
[103] T. Shi, X. Zhang, H. Hao, G. Xie, Influences of random imperfection distribution on the compressive properties of interlocking block wall, Structures 56 (2023) 104875, https://doi.org/10.1016/j.istruc.2023.104875.